

Proceedings of



Symposium 5 Biomaterials

Peter Gumbsch
Editor and Conference Chair

Organized by Fraunhofer-Institute for Mechanics of Materials.
Hosted by University of Freiburg.


Fraunhofer Institut
Werkstoffmechanik


ALBERT-LUDWIGS-
UNIVERSITÄT FREIBURG

Imprint

Papers published in this volume constitute the proceedings of the Third International Conference on Multiscale Materials Modeling. Papers were selected by the program committee for oral or poster presentation. They are published as submitted, in the interest of timely dissemination.

Contact

Fraunhofer Institute for Mechanics of Materials IWM
Woehlerstraße 11
79108 Freiburg
Germany
Phone + 49 761 5142 0
Fax + 49 761 5142 110

The complete proceedings of the conference are available at

Fraunhofer Information-Centre for Regional Planning and Building Construction IRB
P.O. Box 80 04 69, D-70504 Stuttgart
Nobelstrasse 12, D-70569 Stuttgart
Fon +49 (0) 7 11/9 70-25 00
Fax +49 (0) 7 11/9 70-25 07
E-Mail irb@irb.fraunhofer.de
URL www.irb.fraunhofer.de
ISBN-10: 3-8167-7206-4
ISBN-13: 978-3-8167-7206-4

Foreword

Computational modeling of materials behavior by multiscale materials modeling (MMM) approaches is becoming a reliable tool to underpin scientific investigations and to complement traditional theoretical and experimental approaches of component assessment. At transitional (microstructural) scales continuum approaches begin to break down and atomistic methods reach inherent limitations in time and length scale. Transitional theoretical frameworks and modeling techniques are developed to bridge the gap between the different length scales.

Industrial success in high technology fields relies on the possibility to specifically engineer materials and products with improved performance. The success factor is the ability to make these material related developments timely at relatively low-costs. This demands not only the rapid development of new or improved processing techniques but also better understanding and control of material chemistry, processing, structure, performance, durability, and their relationships. This scenario usually involves multiple length and time scales and multiple processing and performance stages, which are usually only accessible via multi-scale / multi-stage modeling or simulation.

In high-payoff, high-risk technologies such as the design of large structures in the aerospace and nuclear industries, the effects of aging and environment on failure mechanisms cannot be left to conservative approaches. Increasing efforts are now focused on advancing MMM approaches to develop new material systems components and devices. Appropriate validation experiments are crucial to verify that the models predict the correct behavior at each length scale. Thus, one of the advantages of these MMM approaches is that, at each scale, physically meaningful parameters are predicted and used in models for subsequent scales, avoiding the use of empiricism and fitting parameters.

Recent interest in nanotechnology is challenging the scientific community to design nanometer to micrometer size devices for applications in new generations of computers, electronics, photonics or drug delivery systems. These new application areas of multiscale materials modeling require novel and sophisticated science-based approaches for design and performance evaluation. Theory and modeling are playing an increasing role to reduce development costs and manufacturing times. With the sustained progress in computational power and MMM methodologies, new materials and new functionalities are increasingly more likely discovered by MMM approaches than by traditional trial and error approach. This is part of a paradigm shift in modeling, away from reproducing known properties of known materials towards simulating the behavior of hypothetical composites as a forerunner to finding real materials with these novel properties.

The MMM 2006 conference provides an international forum for the scientific advances of multiscale modeling methodologies and their applications.

I would like to thank the members of the international advisory committee, the local program committee and particularly the organizing team, the symposium organizers and the session chairs and the University of Freiburg for their engagement and support. Without their hard work and their devotion of time and resources, the Third International Conference Multiscale Materials Modeling would not have been possible.

Finally, I would like to thank our conference sponsors for their financial support: The German Research Foundation DFG, Accelrys Inc., Plansee S.E. and the Ministry of Science, Research and Art, Baden-Württemberg.

Peter Gumbsch
Conference Chair

Conference Committee

International Advisory Committee

Prof. Bacon, David	University of Liverpool, UK
Dr. Baskes, Michael	Los Alamos National Laboratory, USA
Prof. Busso, Esteban	Imperial College, London, UK
Prof. Cale, Timothy S.	Rensselaer Polytechnic Institute, Troy, USA
Dr. Diaz de la Rubia, Tomas	Lawrence Livermore National Lab., USA
Prof. Ghoniem, Nasr	University of California, Los Angeles, USA
Prof. Guo, Xiao	Queens College, London, UK
Prof. Iwata, Shuichi	University of Tokyo, Japan
Prof. Kratochvil, Jan	Technical University, Prague, Czech Republic
Prof. Kremer, Kurt	Max Planck Institute, Mainz, Germany
Dr. Kubin, Ladislav	ONERA-LEM, Chatillon, France
Dr. LeSar, Richard	Los Alamos National Laboratory, USA
Prof. Meguid, Shaker	University of Toronto, Canada
Prof. Needleman, Alan	Brown University, Providence, USA
Prof. Odette, Robert	University of California, Santa Barbara, USA
Prof. Ortiz, Michael	California Institute of Technology, USA
Prof. Pettifor, David	Oxford University, UK
Prof. Phillips, Robert	California Institute of Technology, USA
Prof. Raabe, Dierk	Max Planck Institute, Düsseldorf, Germany
Prof. Shibutani, Yoji	Osaka University, Japan
Dr. Soneda, Naoki	Komae Research Laboratory, Tokyo, Japan
Prof. Suresh, Subra	Massachusetts Institute of Technology, USA
Prof. Tomita, Yoshihiro	Kobe University, Japan
Prof. Van der Giessen, Erik	University of Groningen, Netherlands
Prof. Walgraef, Daniel	Free University of Brussels, Belgium
Dr. Wolf, Dieter	Argonne National Laboratory, USA
Prof. Yip, Sidney	Massachusetts Institute of Technology, USA
Dr. Zinkle, Steve	Oak Ridge National Laboratory, USA

Organizing Committee

M. J. Alava	Helsinki University of Technology, Finland
D. Dimiduk	The Ohio State University, USA
M. Dao	Massachusetts Institute of Technology, USA
M. Doi	University of Tokyo, Japan
C. Elsässer	Fraunhofer IWM, Germany
E. v. d. Giessen	University of Groningen, Netherlands
N. Gov	The Weizmann Institute of Science, Israel
H. J. Herrmann	University of Stuttgart, Germany
R. James	University of Minnesota, USA
K. Kremer	Max Planck Institute for Polymer Research, Germany
J. Korvink	IMTEK, University of Freiburg, Germany
J. Li	The Ohio State University, USA
S. Müller	Max Planck Institute for Mathematics in the Sciences, Germany
A. Paxton	Queen's University, Belfast, UK
M. Payne	University of Cambridge, UK
D. Raabe	Max Planck Institute fuer Eisenforschung, Germany
N. Soneda	Central Research Institute of Electric Power Industry, Japan
M. Zaiser	University of Edinburgh, UK
S. Zapperi	University of Rome, Italy
F. Willaime	Commissariat a l'Energie Atomique (CEA), France
B. Wirth	University of California, Berkeley, USA

Contents

Symposium 5

Multiscale Model of Morphogenesis M. Alber Session 5G	595
Erythrocyte membrane properties revisited T. Auth, N. Gov, S. Safran Session 5L	596
Active Self-Organization Of Myosin II Motors And Actin Filaments A. Bernheim-Groswasser Session 5H	597
Electromechanical coupling in membranes W. Brownell Session 5D	598
Nanomechanics of collagen fibrils M. J. Buehler, E. Loukaides Session 5G	599
Analytical result for the plectonemic response of supercoiled DNA N. Clauvelin, S. Neukirch, B. Audoly Session 5C	605
Molecular-Level Modeling for Erythrocyte Deformation and Related Disease States M. Dao, J. Li, S. Suresh Session 5L	609
Elasticity of gels with active cells R. De Session 6JM	610
Efficient simulation of coarse-grained lipid membranes M. Deserno Session 5L	611
Key roles for elasticity of matrix and cortex - from atomistic simulation to simple thermodynamic model D. Discher Session 5E	614
Mechanical Properties of Icosahedral Virus Capsids G. Gompper, G. Vliegthart Session 5K	615
Membrane fluctuations driven by actin and myosin: waves and quantized division N. Gov, R. Shlomovitz Session 5D	622
Active Transport in Disordered Microtubule Networks R. Granek, J. Klafter Session 5H	623

Vibrations in Proteins: Fractons and Dynamics Detected by Single Molecule Experiments R. Granek, A. Kahana, G. Kenan, M. Elbaum Session 5E	624
Rewiring the T cell signaling network using solid-state nanostructures J. Groves Session 5F	626
How to coarse grain ion potentials in aqueous solutions B. Hess, C. Holm, N. van der Vegt Session 1H	636
Microscopic simulations of macroscopic consequences: fixing the continuum and hybrid methods U. Landman Session 5B	642
Membrane fluctuations around inclusions Ch. D. Santangelo, O. Farago Session 5C	644
Scanning Probe Microscopy of Cytoskeleton Networks. A. Ostafin Session 5F	651
Mechanics of Retrovirus Replication Cycle I. Rousso Session 5K	652
Theory of cell adhesion and elasticity S. Safran, A. Besser, R. De, A. Nicolas, A. Zemel Session 5B	653
Mechanical behavior of single living cells under stretch and compression using micro force sensors T. Saif, S. Yang Session 5G	654
From DNA to chromatin: the physics of DNA compaction H. Schiessel, M. Depken Session 5C	657
Computational Modeling of Cell and Molecular Mechanics and Human Disease States S. Suresh Session 5B	660
Cellular shape formation driven by aggregation of membrane proteins. A. Veksler Session 5D	661

Symposium 5

Biomaterials

Multiscale Model of Morphogenesis

Mark Alber

Department of Mathematics, University of Notre Dame, 255 Hurley Building, 46556-4618 Notre Dame, United States of America

In this talk we present the foundation of a unified, multiscale, object-oriented, three-dimensional biomodelling environment, which allows one to integrate multiple submodels at scales from subcellular to those of tissues and organs. Our current implementation combines a modified discrete model from statistical mechanics, the Cellular Potts Model, with a continuum reaction–diffusion model and a state automaton with well-defined conditions for cell differentiation transitions to model genetic regulation. This environment allows one to rapidly and compactly create computational models of a class of complex developmental phenomena. To illustrate model development, we describe simulations a simplified version of the formation of the skeletal pattern in a growing embryonic vertebrate limb [1,2] as well as somite formation.

1. Chaturvedi, R., C. Huang, B. Kazmierczak, T. Schneider, J. A. Izaguirre, T. Glimm, H.G.E. Hentschel, J. A. Glazier, S. A. Newman, M. Alber [2005], On Multiscale Approaches to 3-Dimensional Modeling of Morphogenesis, *Journal of the Royal Society Interface* 2 3, 237-253.

2. Cickovski, T., C. Huang, R. Chaturvedi, T. Glimm, H.G.E. Hentschel, M. Alber, J. A. Glazier, S. A. Newman, J. A. Izaguirre [2005], A Framework for Three-Dimensional Simulation of Morphogenesis, *IEEE/ACM Transactions on Computational Biology and Bioinformatics* 2 4, 273-288.

Erythrocyte membrane properties revisited

Thorsten Auth¹, Nir Gov¹, Sam Safran¹

¹Weizmann Institute of Science, Department of Materials and Interfaces, 76100 Rehovot, Israel

A fundamental understanding of the shape and fluctuation behaviour of the human erythrocyte is important for applications to medicine and because erythrocytes which are easily isolated in large quantities can serve as relatively simple model systems for more complex cells. Their simplicity arises from the fact that the mechanical properties of the whole cell are completely governed by the properties of the plasma membrane and the adjacent spectrin network. This simplification allows the theory to focus on modelling the composite cell membrane, However, because the total number of molecules exceeds it is not feasible to simulate a complete cell on a molecular level. Multi-scale models that include selected molecular information and which are still able to deal with length scales of the size of the cell are currently the most promising approach for theoretical understanding of the system.

We present a model that couples the fluctuations of the fluid, lipid bilayer with those of the adjacent solid-like, polymerized membrane by excluded volume interactions. The main focus of our research is to examine the consequences of the coupling of these two different types of membranes in order to predict the thermal fluctuations of the erythrocyte membrane. We compare our data with the results of light scattering measurements of the fluctuation spectrum. In a second study, we explicitly model the spectrin filaments as polymer chains. We find an average pressure that acts on the membrane that can be used to calculate the average membrane shape. In addition, we investigate the effects of the ATP concentration on the coupling and on the resulting fluctuations of the coupled lipid and spectrin membranes. Our studies are motivated by the fact that changes in the ATP concentration, which control single-molecule effects, can lead to a significant increase in the amplitudes of the membrane fluctuations.

Active Self-Organization Of Myosin II Motors And Actin Filaments

Anne Bernheim-Groswasser

Ben-Gurion University of the Negev, P.O. Box 653, 84105 Beer-Sheva, Israel

The cytoskeleton plays an important role in many subcellular processes as cell division, and cell locomotion. Depending on the specific task, the appropriate cytoskeletal structure has to be formed. Biophysical studies have indicated that the formation of cytoskeletal structures can be achieved by self-organization of cytoskeletal components. Switching between different such structures could thus be obtained by simple modifications of the participating components, i.e., the formation of the contractile ring during cell division from an initially homogenous isotropic actin cortex could have its origin in the activation of molecular motors and an increased polymerization and depolymerization activity of actin filaments. Here we study the active self-organization of actin filaments by myosin II molecular motors from an isotropic solution of actin filaments or monomers. Depending on the system composition rings, bundles or active networks are formed. Similar substructures are also observed in vivo.

Electromechanical coupling in membranes

William Brownell

Baylor College of Medicine, Department of Otolaryngology - H&N Surgery, One Baylor Plaza, 77030 Houston, United States of America

Biological membranes are a rich mixture of lipids, proteins, and other molecules. Lipids are about 100 times more numerous than proteins. The self-assembling lipid bilayer accounts for the thinness of the membrane (typically ~ 5 nm) and its ability to sustain a transmembrane electrical field of > 10 MV/m. This powerful electric field results from the fact that the membranes of living cells are polarized (the inner surface is more negative than the outer) and electrochemical gradients across the membrane are maintained by ion pumps. We show experimental evidence that membranes can harness the energy in the transmembrane electric field and perform useful work (such as counteracting viscous damping in the inner ear or mixing an unstirred layer). Thin cylinders (tethers) of membrane are formed and the axial force resulting from changes in the electric field measured using optically trapped beads. Hyperpolarizing potentials increase and depolarizing potentials decrease the electromechanical force. Tether movements can be measured in response to sinusoidal voltage signals at acoustic frequencies > 3 kHz. Sinusoidal force production is a function of tether length and holding potential. No single model is currently able to explain the nano-MEMS properties of the biological membrane. A mesoscopic continuum approach is suggested by the fact that surface tension holds the membrane together. The relatively feeble scaling of surface tension makes it progressively more important in the micrometer and nanometer regimes where it can dominate. The modulation of surface tension by an electric field across a mercury/saline solution interface was first described by Lippmann and has recently been used as the basis for microfluidic motors. More atomistic approaches suggest a role for the orientation of electrical dipoles. The ability of different models to explain electromechanical coupling in membranes will be discussed.

Nanomechanics of collagen fibrils

Markus J. Buehler^{1,*} and Evaripides G. Loukaides¹

¹ Department of Civil and Environmental Engineering, Massachusetts Institute of Technology, Cambridge, MA, 02139, USA

* Corresponding author, email: mbuehler@MIT.EDU

ABSTRACT

Collagen is a protein material with superior mechanical properties, consisting of collagen fibrils composed of a staggered array of ultra-long tropocollagen molecules. Here we use a fully atomistic based mesoscopic model that enables studying the elastic and fracture behavior of individual tropocollagen molecules, as well as the mechanics of assemblies of tropocollagen molecules into collagen fibrils (M.J. Buehler, *PNAS*, 2006). Using a simplistic representation of a collagen fibril based on a staggered assembly of tropocollagen molecules, we show that Young's modulus decreases with increasing number of tropocollagen fibrils, illustrating the scale dependent properties of collagen. Our results show qualitative agreement with experimental results (N. Sasaki and S. Odajima, *J. of Biomechanics*, 1996), who also observed a decrease of Young's modulus comparing a single tropocollagen molecule to collagen fibril.

1. Introduction

Materials found in Nature often feature hierarchical structures ranging from the atomistic, molecular to the macroscopic scales [1-5]. Many biological materials found in living organisms, often protein-based, feature a complex hierarchical design.

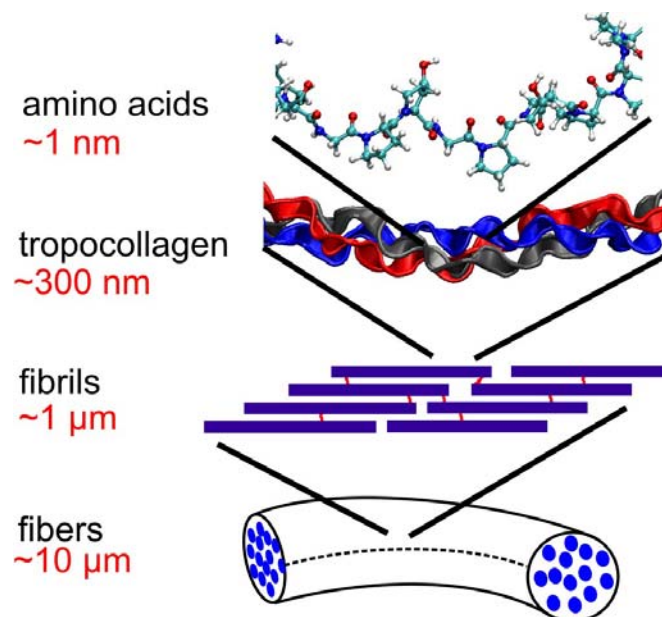


Figure 1: Hierarchical design of collagen. Here we focus on the difference of the material properties between individual TC molecules and collagen fibrils.

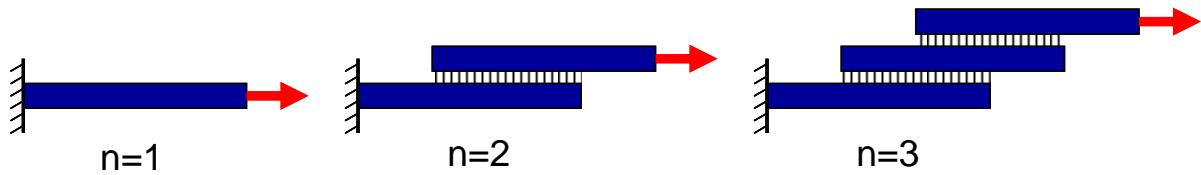


Figure 2: Schematic of the stacking pattern used in our simulation. The first atom in the first molecule is held in place while a force F acts on the other end. The largest width of the assembly in the direction orthogonal to the applied load is taken as the cross-sectional area A . The length of each TC molecule is 300 nm, close to experimental values.

Collagen, the most abundant protein on earth, is a fibrous structural protein with superior mechanical properties, and provides an intriguing example of a hierarchical biological nanomaterial [4, 6-18]. Collagen consists of tropocollagen (TC) molecules that have lengths of $L \approx 280$ nm with roughly 1.5 nm in diameter, leading to an aspect ratio of around 190 [6, 7, 9, 18-20]. Staggered arrays of TC molecules form fibrils, which arrange to form collagen fibers (Figure 1).

Collagen plays an important role in many biological tissues, including tendon, bone, teeth or cartilage [6, 7, 13, 15, 19, 21]. Severe mechanical tensile loading of collagen is significant under many physiological conditions, as in joints and in bone [22, 23]. Despite significant research effort over the past decades, the geometry, the typical length scales found in collagen fibrils, as well as the deformation mechanisms under mechanical load, and in particular its relation to the molecular and intermolecular properties are not well understood well. Moreover, the limiting factors in strength of collagen fibrils, and the origins of toughness remain largely unknown. Here we report studies regarding the mechanics of individual tropocollagen molecules and assemblies of TC molecules into collagen fibrils, with a particular focus on changes in Young's modulus [20]. Using molecular modeling, we show that Young's modulus decreases from a single TC molecule to an assembly of TC molecules into a collagen fibril.

2. Computational model

We use a mesoscale bead model of TC molecules, as described in [24]. We assemble the TC molecules in the manner shown in Figure 2, with a varying number of molecules, from one to three molecules. For each case, we perform a steered molecular dynamics calculation using the LAMMPS molecular dynamics code.

From the force-displacement data, we calculate Young's modulus by considering the small-deformation linear elastic regime. With F being the applied force, and A as the cross-sectional area of the bundle, the stress is given by

$$\sigma = \frac{F}{A}. \quad (1)$$

The strain is defined as

$$\varepsilon = \frac{\Delta L}{L}, \quad (2)$$

with ΔL as the increase in length due to applied force, and L the initial length of the molecular assembly. Young's modulus is given by

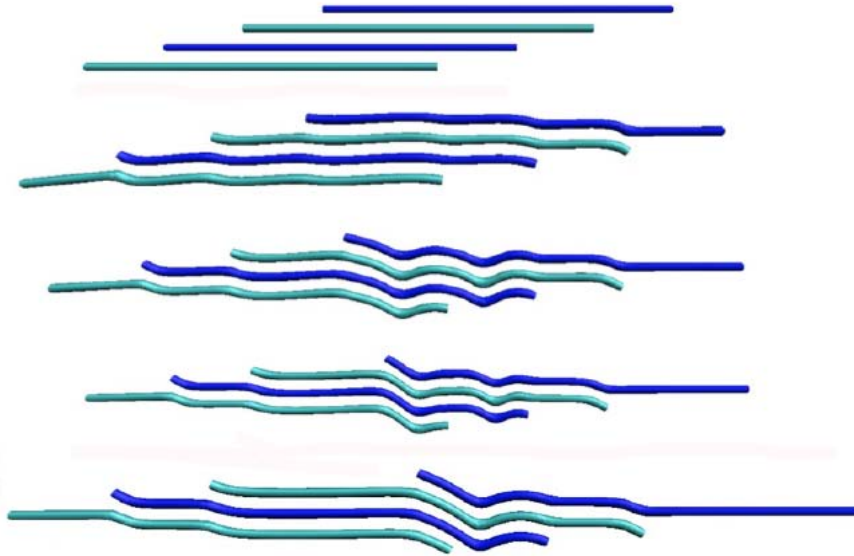


Figure 3: Deformation mechanics of an assembly of four TC molecules. The frames were rendered using VMD [25]. To improve the visualization, the x -component is shown compressed by a factor of 10. Note that this figure depicts permanent (plastic) deformation, beyond the elastic regime. For the analysis of Young's modulus, we only consider the reversible deformation without intermolecular slip.

$$E = \frac{\Delta\sigma}{\Delta\varepsilon}. \quad (3)$$

The cross-sectional area is given by

$$A = nD^2, \quad (4)$$

where n is the number of molecules at the largest cross-section in the molecule, and $D \approx 15.2 \text{ \AA}$ is the distance between two TC molecules as obtained by full-atomistic studies [26]. We only consider assemblies of up to $n = 5$ molecules, since there is no axial overlap for more molecules (between the first and fifth or more staggered copy), leading to a constant cross-sectional area. There are no cross-links between tropocollagen molecules.

3. Computational results

Figure 3 shows the results of a molecular simulation of an assembly of $n = 4$ molecules. As reported in earlier studies [24], deformation is dominated by intermolecular shear. Figure 4 depicts the computed values of Young's modulus. It is evident that Young's modulus decreases with an increase of the number of molecules. The plot also includes experimental results of the elasticity of a single TC molecule and the elasticity of a collagen fibril [20].

Figure 5 depicts a direct comparison of the stress-strain behavior of a single TC molecule and a collagen fibril, as observed in experiment [20]. In the plot, we also include the stress-strain slopes obtained by molecular modeling (note that the slope of the single TC molecule is renormalized to match experimental results).

4. Discussion and conclusion

The results indicate that our model is capable of reproducing experimental observation of reduction of Young's modulus, with increasing number of TC molecules. In contrast to earlier attempts of describing the mechanics of collagen, our model is free of empirical parameters. All parameters in the mesoscale model are obtained from full-atomistic modeling.

The reduction of Young's modulus with increasing number of molecules can be explained based on a simple model that treats the fibril model (Figure 2) as a combination of springs. We assume that there exist two springs with spring constants k_1 and k_2 , where $k_1 > k_2$ (atomistic modeling suggests a ration of 5 to 10 for k_1/k_2). The spring constant k_1 describes the elastic response of an individual TC molecule, whereas k_2 describes the intermolecular spring. The collagen fibril with n molecules can be described as a serial combination of springs, with an effective spring constant

$$k_{eff} = \left(\frac{n}{k_1} + \frac{n-1}{k_2} \right)^{-1}. \quad (5)$$

Note that there are n stiff springs with k_1 , and $n-1$ soft (intermolecular) springs with k_2 . The stress due to displacement Δu is given by $\sigma = k_{eff} \Delta u / A$. Young's modulus is defined as σ / ε , where $\varepsilon = \Delta u / u$. Since $A \sim n$ (see equation (4)) and $u \sim n$ (constant axial staggering displacement, and thus $u = u_0 + (1 - \alpha)u_0(n-1)$, where α is the ratio of axial shift between two neighboring TC molecules, chosen to be 0.77), Young's modulus is proportional to k_{eff} :

$$E \sim k_{eff}. \quad (6)$$

Equation (5) provides a qualitative explanation for the reduction of modulus with increasing number of molecules. However, this simple model overestimates the drop in modulus compared with simulation and experiment, since k_{eff} decreases when n increases.

Our results help to explain the experimental observation of a reduced modulus of collagen fibrils compared to individual molecules.

5. Acknowledgements

EL acknowledge support from MIT's UROP program, and MJB acknowledges support from the MIT's CEE department.

6. References

1. Arzt, E., S. Gorb, and R. Spolenak, *From micro to nano contacts in biological attachment devices*. P. Natl. Acad. Sci. USA, 2003. **100**: p. 10603-10606.
2. Gao, H., et al., *Materials become insensitive to flaws at nanoscale: Lessons from nature*. P. Natl. Acad. Sci. USA, 2003. **100**(10): p. 5597-5600.
3. Gupta, H.S., et al., *Nanoscale deformation mechanisms in bone*. Nano Letters, 2005. **5**(10): p. 2108-2111.
4. Jager, I. and P. Fratzl, *Mineralized collagen fibrils: A mechanical model with a staggered arrangement of mineral particles*. Biophysical Journal, 2000. **79**(4): p. 1737-1746.

5. Peterlik, H., et al., *From brittle to ductile fracture of bone*. Nature Materials, 2006. **5**(1): p. 52-55.
6. Bozec, L. and M. Horton, *Topography and mechanical properties of single molecules of type I collagen using atomic force microscopy*. Biophysical Journal, 2005. **88**(6): p. 4223-4231.
7. Bhattacharjee, A. and M. Bansal, *Collagen structure: The Madras triple helix and the current scenario*. Iubmb Life, 2005. **57**(3): p. 161-172.
8. Anderson, D., *Collagen Self-Assembly: A Complementary Experimental and Theoretical Perspective*. 2005, University of Toronto: Toronto, Canada.
9. Sun, Y.L., et al., *Stretching type II collagen with optical tweezers*. Journal Of Biomechanics, 2004. **37**(11): p. 1665-1669.
10. An, K.N., Y.L. Sun, and Z.P. Luo, *Flexibility of type I collagen and mechanical property of connective tissue*. Biorheology, 2004. **41**(3-4): p. 239-246.
11. Lees, S., *Mineralization of type I collagen*. Biophysical Journal, 2003. **85**(1): p. 204-207.
12. Sun, Y.L., et al., *Direct quantification of the flexibility of type I collagen monomer*. Biochemical And Biophysical Research Communications, 2002. **295**(2): p. 382-386.
13. Hellmich, C. and F.J. Ulm, *Are mineralized tissues open crystal foams reinforced by crosslinked collagen? - some energy arguments*. Journal Of Biomechanics, 2002. **35**(9): p. 1199-1212.
14. Waite, J.H., X.X. Qin, and K.J. Coyne, *The peculiar collagens of mussel byssus*. Matrix Biology, 1998. **17**(2): p. 93-106.
15. Borel, J.P. and J.C. Monboisse, *Collagens - Why Such A Complicated Structure*. Comptes Rendus Des Seances De La Societe De Biologie Et De Ses Filiales, 1993. **187**(2): p. 124-142.
16. Lees, S., *Possible Effect Between The Molecular Packing Of Collagen And The Composition Of Bony Tissues*. International Journal Of Biological Macromolecules, 1987. **9**(6): p. 321-326.
17. Fratzl, P., et al., *Structure and mechanical quality of the collagen-mineral nanocomposite in bone*. Journal Of Materials Chemistry, 2004. **14**(14): p. 2115-2123.
18. Hulmes, D.J.S., et al., *Radial Packing, Order, And Disorder In Collagen Fibrils*. Biophysical Journal, 1995. **68**(5): p. 1661-1670.
19. Puxkandl, R., et al., *Viscoelastic properties of collagen: synchrotron radiation investigations and structural model*. Philosophical Transactions Of The Royal Society Of London Series B-Biological Sciences, 2002. **357**(1418): p. 191-197.
20. Sasaki, N. and S. Odajima, *Elongation mechanism of collagen fibrils and force-strain relations of tendon at each level of structural hierarchy*. Journal Of Biomechanics, 1996. **29**(9): p. 1131-1136.
21. Bozec, L., et al., *Atomic force microscopy of collagen structure in bone and dentine revealed by osteoclastic resorption*. Ultramicroscopy, 2005. **105**(1-4): p. 79-89.
22. Nalla, R.K., et al., *Mechanistic aspects of fracture and R-curve behavior in human cortical bone*. Biomaterials, 2005. **26**(2): p. 217-231.
23. Ritchie, R.O., et al., *Characteristic dimensions and the micro-mechanisms of fracture and fatigue in 'nano' and 'bio' materials*. International Journal Of Fracture, 2004. **128**(1-4): p. 1-15.
24. Buehler, M.J., *Nature designs tough collagen: Explaining the nanostructure of collagen fibrils*. P. Natl. Acad. Sci. USA, in press.
25. Humphrey, W., A. Dalke, and K. Schulten, *VMD: Visual molecular dynamics*. Journal Of Molecular Graphics, 1996. **14**(1): p. 33.
26. Buehler, M.J., *Atomistic and continuum modeling of mechanical properties of collagen: Elasticity, fracture and self-assembly*. J. Mater. Res., in press.

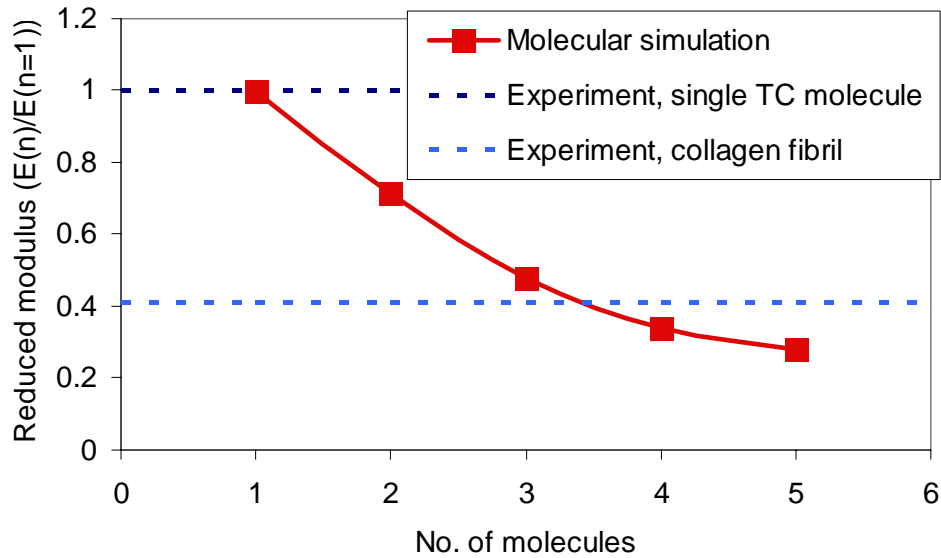


Figure 4: Variation of Young’s modulus E with respect to the number of molecules in the system. The results are normalized with respect to the total value obtained by stretching a single TC molecule. The results show a clear decrease of Young’s modulus with increasing number of molecules. Our results indicate that the modulus decreases with an increase in number of molecules, approaching a value close to the reduced modulus of a fibril, as seen in experiment [20].

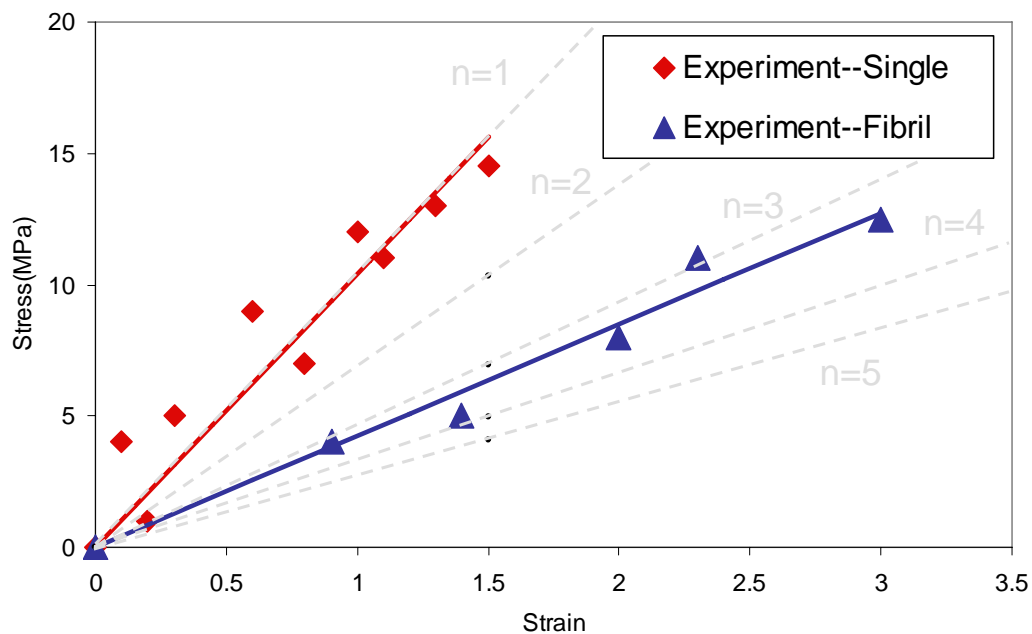


Figure 5: Experimental result of the stress-strain behavior of a single TC molecule (red squares) and a collagen fibril (blue triangles), as reported in [20]. The plot also contains the results of our molecular modeling, showing that the results for a larger number of molecules fall into the range of experimental results, clearly indicating the drop of modulus with increasing number of molecules. The slope of the modeling result corresponding to the single TC molecule is renormalized to match experimental results as a reference point.

Analytical Results For The Plectonemic Response Of Supercoiled DNA

Nicolas Clauvelin, Sébastien Neukirch, Basile Audoly

**Laboratoire de Modélisation en Mécanique,
CNRS & Université Pierre et Marie Curie
4 place Jussieu, 75005 Paris, France
clauvelin@lmm.jussieu.fr**

ABSTRACT

The DNA molecule is modeled as an elastic rod with bending and twisting rigidities, subjected to external tension and twist applied at one end, the other end being clamped. We study the plectonemic equilibrium of such a rod, taking into account the impenetrability constraint. Numerical solutions of this boundary value problem have previously shown that purely elastic models can reproduce the supercoiling response of the DNA molecule. Using a variational approach, we derive analytical formulae for the elastic response of the filament, and extend former numerical results.

1. Introduction

It is widely known that mechanical properties of the DNA molecule play an important role in the biology of cell, but at present we only have an imprecise view of the way DNA responds to various constraints. There is currently an upsurge of interest in this question as nanotechnologies make it possible to apply forces onto an isolated DNA filament.

A typical loading that can be performed experimentally on a double strand of DNA is shown in Fig 1: a DNA molecule is fixed at one end on a glass pane while the other end is attached to a magnetic bead [1]. By using a magnet, it is possible to pull on the bead while twisting it around a vertical axis [2]. For a fixed pulling force, the molecule wraps around itself in a helical way, when the rotation angle of the bead exceeds a threshold value: the resulting structure is called a plectonem. These experiments can be done for different pulling forces, molecule contour lengths or salt concentrations.

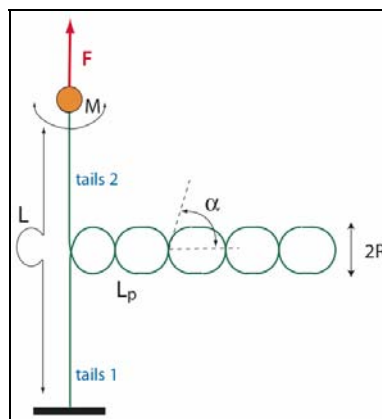


Figure 1. Simplified view of the experimental setup

2. Elastic model for the plectonemic regime

We first investigate the equilibrium behavior of an elastic rod under the constraints described above. The rod, with bending rigidity K_0 , and twisting rigidity K_3 , is considered inextensible, with a constant circular cross section of radius a , and a total contour length L . We note s the arclength with $s=0$ for the end fixed to the glass and $s=L$ for the other end. The external loads are the pulling force $F(L)$ and the torsional moment $M(L)$.

2.1 Plectonems geometry

To analyze the mechanical response of plectonems we make an ansatz on the geometry of the twisted filament, relevant to large applied twist: we assume that the plectonems can be assimilated to two identical and perfect helices (each one of these helices is itself a double strand of DNA), and we also suppose that curvature and twist are uniform in the plectonemic part. In the tails we further consider the twist to be uniform and the curvature to vanish, and we neglect both the end loop of the plectonems and the region connecting the tails and the plectonemic part.

We parametrize the rod with Euler angles, and take into account material twist as well as geometrical torsion, which add up to give the total twist [3]. At the equilibrium the plectonems are described by five variables: the plectonemic radius R , the opening angle α , the value of the material twist ζ_p in the plectonems, the length L_p of the plectonemic region, and the material twist value ζ_t in the tails. We have for total curvature and twist the following expressions (where $\varepsilon=\pm 1$ stands for the chirality):

$$\begin{aligned} \kappa(s) &= \begin{cases} 0 = \kappa_t & \text{if } s \in \text{tails} \\ \frac{\sin^2 \alpha}{R} = \kappa_p & \text{if } s \in \text{plecto} \end{cases} \\ \tau(s) &= \begin{cases} \zeta_t = \tau_t & \text{if } s \in \text{tails} \\ \zeta_p + \varepsilon \frac{\sin \alpha \cos \alpha}{R} = \tau_p & \text{if } s \in \text{plecto} \end{cases} \end{aligned} \quad (1)$$

We model the self-contact of the filament by a hard-wall potential. Geometric impenetrability implies that the two helices contact along a straight line, as long as the opening angle is less than $\pi/4$. In this case the plectonemic radius equals to the circular cross section of the rod.

2.2 Potential energy of the rod

We now derive the potential energy of the elastic rod, which is the sum of three terms: the elastic energy, the work done by external loads, and the contact condition:

$$\begin{aligned} V(\alpha, R, L_p, \zeta_t, \zeta_p) &= \frac{K_0 L_p}{2} \kappa_p^2 + \frac{K_3 (L - L_p)}{2} \tau_t^2 + \frac{K_3 L_p}{2} \tau_p^2 \\ &\quad - F(L)(L - L_p) - M(L)((L - L_p)\zeta_t + L_p\zeta_p) \\ &\quad + \lambda(R - a) \end{aligned} \quad (2)$$

where the strain elastic energy is the sum of the square of the curvature and the square of the twist, and the external force works again extension and the external moment works again rotation. Finally the contact constraint is represented with a Lagrange multiplier, λ .

2.3 Results

We seek extrema of Eqn (2) with regard to the five variables. Euler-Lagrange minimization with respect to the twist variables ζ_p and ζ_t yields $K_3\zeta_t = M(L)$ and $K_3[\zeta_p + \epsilon \sin 2\alpha/(2R)] = M(L)$, which show that the internal moment $M(s)$ is constant along the filament, and takes the value $M(L)$ imposed by the loading, both in the tails and in the plectonemic part.

Minimization with respect to the opening angle gives the value of this internal moment:

$$M(L) = -2\epsilon \frac{K_0 \cos \alpha \sin^3 \alpha}{R \cos 2\alpha} \quad (3)$$

For the variable R we obtain the expression of the contact pressure in the rod:

$$p = \frac{K_0 \sin^4 \alpha}{R^3 \cos 2\alpha} \quad (4)$$

Finally for the L_p variable we find the relation between the pulling force and the plectonemic variables:

$$F(L) = \frac{K_0}{R^2} \sin^4 \alpha \left(\frac{1}{2} + \frac{1}{\cos 2\alpha} \right) \quad (5)$$

Notice that the value of R is fixed by the condition of hard-wall contact $R=a$. With the help of Eqn (5) we obtain the value of α since the value of $F(L)$ is fixed, and we have checked that this set of equations accurately describes the numerical results of [4].

3. Application to the DNA molecule

In order to apply our model to DNA molecules we must consider the electrostatic effects due to the bare charge of DNA and to the counter-ions of the solution. Since the inter-strand distance is of the order of the Debye screening length the Debye-Hückel approximation, leading to the linear Poisson-Boltzmann equation, is not valid in the case we consider. The study of the non-linear case is, according to our knowledge, only possible numerically, and therefore does not yield any analytical expression. For example [5] investigates the potential created by a charged cylinder, and [6] consider helical geometry but within the linear approximation.

We choose to avoid these difficulties by calculating an *effective radius* of the DNA molecule in the plectonemic regime. By *effective radius* we mean the radius that the molecule must have for acting as a non-charged rod-like polymer. In fact it boils down to determinate the radius of the circular cross section introduced in the elastic model with hard-wall contact. We give in Fig 2 the effective radius as a function of the pulling force. These results are extracted from experimental data, as explained in [4], provided by G. Charvin and V. Croquette (LPS – ENS, Paris), on a dsDNA molecule of 11kbp.

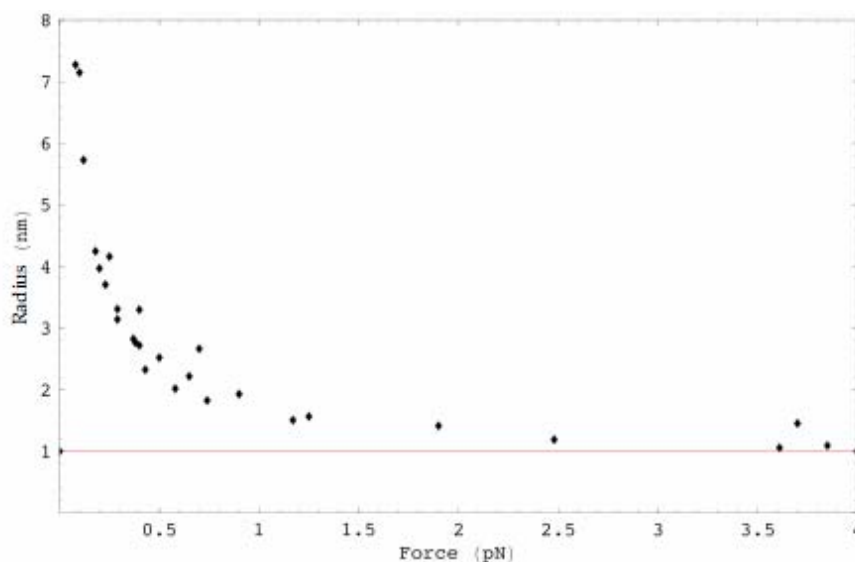


Figure 2. Effective radius versus pulling force

Fig 2 shows that at low forces the effective radius of the molecule is about 1nm, which is in good agreement with ordinary values of the core radius of dsDNA (from 0.9nm to 1.2nm). The increase of the effective radius can be interpreted in term of the Manning condensation process [7], although it is probably not the only effect to take into account. Experimental studies on plasmids at zero force [8] shows that the salt concentration influences the effective radius of the DNA molecule in a manner still not understood.

Acknowledgements

We thank G. Charvin and V. Croquette from the Laboratoire de Physique Statistique de l'ENS (Paris, France) for kindly providing experimental data on the DNA supercoiling.

References

- [1] Smith, S. B. and Finzi, L. and Bustamante, C., *Science*, **258** (1992) pp 1122–1126.
- [2] Strick, T. R. and Allemand, J.-F. and Bensimon, D. and Bensimon, A. and Croquette, V., *Science*, **271** (1996) pp 1835–1837.
- [3] Van Der Heijden, G. H. M. and Thompson, J. M., *Nonlinear Dynamics*, **21** (2000) pp 71–99.
- [4] Neukirch, S., *Physical Review Letters*, **93**#19 (2004) 198017.
- [5] Stigter, D., *J. Coll. And Interf. Sci.*, **53**#2 (1975) pp 296–306.
- [6] Ubbink, J. and Odijk, T., *Biophys. J.*, **76** (1999) pp 2502–2519.
- [7] Manning, G. S., *J. Chem. Phys.*, **51**#3 (1969) pp 924–938.
- [8] Rybenkov, V. V. and Vologodskii, A. V. and Cozzarelli, N. R., *Nucl. Acids Res.*, **25**#7 (1997) pp 1412–1418.

Molecular-Level Modeling for Erythrocyte Deformation and Related Disease States

Ming Dao¹, Subra Suresh¹, Ju Li²

¹MIT, 77 Massachusetts Ave, Cambridge, United States of America

²The Ohio State University, 2041 college Road, 43210 Columbus, United States of America

The mechanical properties of erythrocytes (red blood cells) influence strongly their biological functions and the onset, progression and consequences of a number of human diseases. The hyperelasticity characteristics of erythrocyte subjected to finite-deformation stretching is studied at the spectrin level by molecular dynamics as well as at the continuum level by finite-element modeling. We have further developed an on-the-fly homogenization scheme for studying the mechanics of living cells that comprise 2D/3D molecular networks as structural bases---Molecular Potential Finite Element Method (MPFEM). For the spectrin network that provides membrane shear elasticity, we use the worm-like chain (WLC) potential for single spectrin molecular response. Connections among molecular structure, cell mechanical deformation and disease states related to heredity spherocytosis and Plasmodium falciparum malaria are discussed.

Elasticity of gels with active cells

Rumi De¹, Assaf Zemel¹, Samuel A. Safran¹

¹Department of Materials and Interfaces, Weizmann Institute of Science, 76100 Rehovot, Israel

Mechanical forces acting externally on entire tissues, or generated internally by the contractile activity of individual cells within a tissue, play an important regulatory role in many physiological processes, including: bone and muscle growth, wound healing, angiogenesis and others. Understanding the response of single cells embedded in gel matrices to mechanical loadings, and their behaviour as a collective, is important not only for basic biological science but also for the rational design of artificial tissues. Individual cells possess specific mechanisms that enable them to sense and respond to changes in their mechanical environment. By pulling on their environment, cells sense rigidity gradients, boundaries and strain. Many cell types respond to these signals by actively adjusting cell polarity. On a macroscopic level, the forces generated by a collection of cells in a tissue significantly alter the overall elastic response of the system.

We predict the response of cells in a three dimensional elastic medium to externally applied strain fields. The cells are modelled as polarizable, elastic force dipoles that can change their orientation in response to the local elastic stress. We model the ensemble of cells by an extension of the treatment of dielectric response of polar molecules. We introduce the elastic analogy of the frequency-dependant dielectric function of the medium that allows us to predict the average cell polarization and orientational order, the effective material constants, and the dynamical response to time-varying cyclic loadings.

Efficient simulation of coarse-grained lipid membranes

Markus Deserno

Max-Planck-Institut für Polymerforschung, Ackermannweg 10, 55118 Mainz, Germany

ABSTRACT

Lipid bilayers are one of the key materials used by nature. In the range of a few tens up to a few hundred nanometers a simulational approach typically resorts to coarse-grained models; however, once the membranes start to bend strongly, the presence of solvent becomes a severe obstacle, since it occupies the bulk phase and thus consumes most of the simulation time. Devising solvent-free models has therefore been a longstanding goal, which surprisingly has proved far more challenging than researchers had anticipated initially, and significant progress has only been made in the past few years. This contribution briefly describes a recently developed model that has the advantage of being particularly simple, robust, and still physically very appealing.

1. Introduction

On the length scale of nanometers lipid membranes appear as dense aggregates of amphiphilic lipid molecules, on the length scales of microns they appear as elastic two-dimensional fluid surfaces. Both regimes have long been treated with computational or analytical techniques, such as all-atom Molecular Dynamics for the small scale and continuum Helfrich theory for the large scale. But on scales of many tens to a few hundred nanometers neither approach is optimal. In this regime so-called coarse-grained lipid models have been introduced, which reflect only very few aspects of a lipid's molecular structure, maybe only its amphiphilic character. This way fewer degrees of freedom are required for the lipid, hence more lipids can be simulated, hence longer length scales are reachable.

On mesoscopic scales interesting membrane problems frequently involve bilayers which are no longer flat. But once the surface bends into the third dimension, it hits us with a vengeance that most of the simulation box is filled with solvent (usually water), not with the membrane we initially set out to study. The obvious desire to eliminate this computational burden in situations in which the solvent is no significant part of the physics has motivated people to look for coarse-grained lipid models which work without the need of an explicit (equally coarse grained) solvent, but things have turned out to be more complicated than expected: While it proved rather easy to replace the solvent by some effective attractive interactions between the hydrophobic lipid tails, the general finding in early days seemed to be that when membranes form, then they are solid-like ("gel-phase"), while fluid aggregates are unstable with respect to thermal undulations [1].

The deeper reason for this difficulty is this: Membranes are self-assembled structures; the cohesive energy driving their aggregation is of the order of the thermal energy. Hence, the very same energies which enable fluid membranes also threaten their existence. For this reason the question "What is the right choice for a cohesive energy?" is a bit more subtle than in the case of pre-assembled mesoscopic structures, such as for instance polymers (for a detailed account see [1]). A variety of solutions have been proposed recently (see the Review by Brannigan *et al.* [2]), but only very recently working models relying on simple pair potentials with very few tuning parameters have been proposed [3,4].

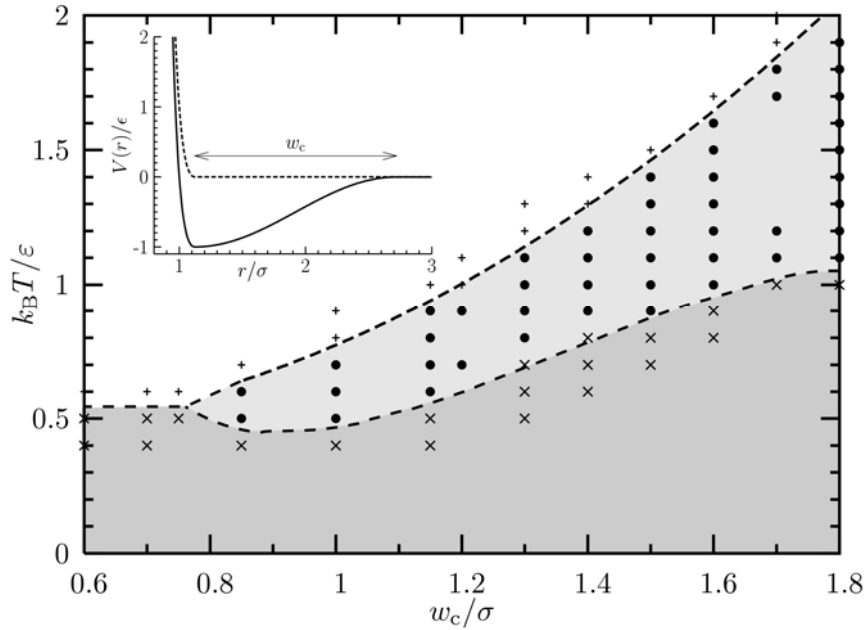


Figure 1: Phase diagram of the bilayer model for tensionless planar membranes in the plane of temperature and potential range (see Ref. [3,5]).

2. Coarse-grained solvent-free model based on broad tail attractions

The lipid model we have recently proposed [3,5] uses three spheres in a row to represent a single lipid: One hydrophilic head-bead and two subsequent hydrophobic tail-beads; this trimer of beads is stiffened by an effective bending-spring. All spheres have an excluded volume, modeled by the repulsive part of a Lennard-Jones potential. Aggregation is driven by a tail-attraction, and the key to permitting a fluid bilayer phase lies in the use of a sufficiently long-ranged potential minimum, such that lipid rearrangements – necessary to enable the entropy of the fluid phase – can be excited thermally. Specifically, we use the simple pair-potential $U(r) = -\varepsilon \cos^2[\pi(r - r_c)/2w_c]$ for $r_c \leq r \leq r_c + w_c$, where r_c is the point where the Lennard-Jones repulsion sets in, w_c is the range of the “cosine-attraction”, and ε is the unit of energy. Other functional forms give qualitatively similar results [5].

Depending on w_c/σ (where σ is the tail-bead diameter) and $k_B T/\varepsilon$ the system is either

- in an unaggregated gas-phase for sufficiently large temperature T ,
- in a gel-phase (solid) for sufficiently small T ,
- or in a fluid phase for intermediate T and sufficiently large w_c .

For a bilayer under zero applied tension this phase behavior is illustrated in Fig. 1.

Specifically, in the fluid phase a variety of relevant bilayer properties can be measured [5], such as the order parameter, monolayer-overlap, the area per lipid, and bilayer rigidity. The latter can be obtained from the low- q -behavior of the fluctuation spectrum, which under zero tension is given by $\langle |h_q|^2 \rangle = k_B T / L^2 \kappa q^4$, and one finds bending rigidities κ at least within the range $3 \dots 30 k_B T$, the correct range for typical phospholipid bilayers [3,5].

By changing the size of the head-bead, different lipid curvatures can be accessed [6]. This way the entire range of aggregate shapes – spherical micelles, unbranched and branched cylindrical micelles, and bilayers – can be accessed, see Fig. 2. One expects that lipids with different aspect ratios sense the curvature of the monolayer in which they are embedded differently, hence the local composition of mixtures of differently shaped lipids should

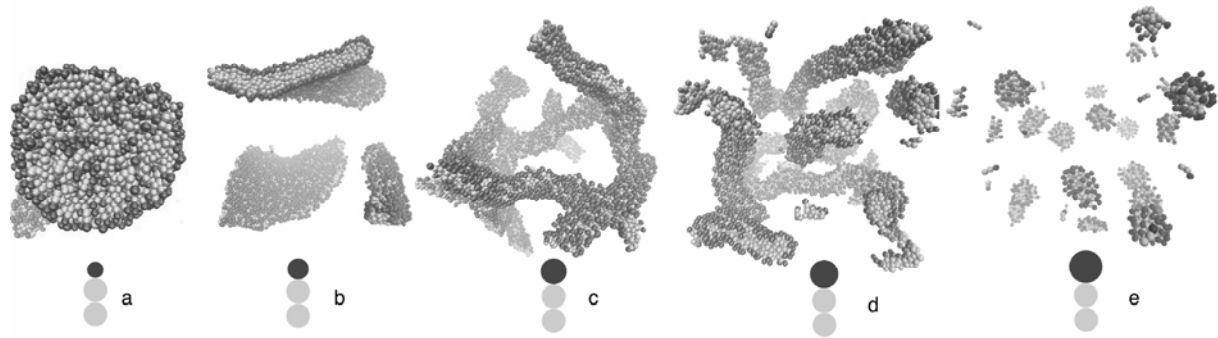


Figure 2: Example of a sequence of aggregate shapes upon changing the ratio between head- vs. tail-bead size (or, equivalently, the Israelachvili/Mitchell/Ninham packing parameter P) as follows: a:0.7($P=1.4$), b:0.9($P=0.83$), c:1.1($P=0.55$), d:1.2($P=0.46$), e:1.4($P=0.33$). Details see Ref.[6].

depend on the local state of curvature. This can indeed be quantified and explained using simple analytical tools [6]. The effect is small, though, implying that its use for the purpose of lipid sorting would require it to go in hand with other mechanisms, such as for instance shape-triggered lipid demixing.

Acknowledgements

The author would like to thank Ira Cooke, Kurt Kremer, Gregoria Illya, Benedict Reynolds, and Vagelis Harmandaris for many inspired contributions. Financial support by the German Science Foundation under Grand De775/1-3 is also gratefully acknowledged.

References

- [1] M. Deserno, in: *Computer Simulation Studies in Condensed Matter Physics XIX*, ed. by D.P. Landau, S.P. Lewis, and H.B. Schüttler, Springer, Heidelberg (2006).
- [2] G. Brannigan, L.C.-L. Lin, and F.L.H. Brown, *Implicit solvent simulation models for biomembranes*, *Eur. Biophys. J.* **35**, 104 (2006).
- [3] I.R. Cooke, K. Kremer, and M. Deserno, *Tunable generic model for fluid bilayer membranes*, *Phys. Rev. E* **72**, 011506 (2005).
- [4] G. Brannigan, P.F. Phillips, and F.L.H. Brown, *Flexible lipid bilayers in implicit solvent*, *Phys. Rev. E* **72**, 011915 (2005).
- [5] I.R. Cooke and M. Deserno, *Solvent-free model for self-assembling fluid bilayer membranes: Stabilization of the fluid phase based on broad attractive tail potentials*, *J. Chem. Phys.* **123**, 224710 (2005).
- [6] I.R. Cooke and M. Deserno, *Coupling between lipid shape and membrane curvature*, *Biophys. J.* **91**, 487 (2006).

Key roles for elasticity of matrix and cortex - from atomistic simulation to simple thermodynamic model

Dennis Discher

University of Pennsylvania, 112 Towne Bldg, 19104 Philadelphia, United States of America

Cellular disease and differentiation are often thought of in strictly molecular terms, but we will present several examples of where a more continuum concept of elasticity at that level and certainly higher are key to understanding. Steered molecular dynamics of protein extension (on the protein, spectrin) has been studied as a function of temperature and elasticity changes shows good correlation with disease causing mutations. Analogous models to the simplest ones applied in electrophysiology are then developed for understanding how cells probe and respond to matrix elasticity. The experimental results highlight novel physical mechanisms in differentiation while the modeling perhaps points the way toward simple thermodynamic approaches to an otherwise complicated mechanical problem.

Mechanical Properties of Icosahedral Virus Capsids

G. A. Vliegenthart and G. Gompper

Institut für Festkörperforschung,
Forschungszentrum Jülich, D-52425 Jülich, Germany

ABSTRACT

Virus capsids are self-assembled protein shells in the size range of 10 to 100 nanometers. The shells of DNA-viruses have to sustain large internal pressures while encapsulating and protecting the viral DNA. We employ computer simulations to study the mechanical properties of crystalline shells with icosahedral symmetry that serve as a model for virus capsids. The shells are positioned on a substrate and deformed by a uni-axial force exerted by a small bead. We predict the elastic response for small deformations, and the buckling transitions at large deformations. Both are found to depend strongly on the number N of elementary building blocks (capsomers), and the Föppl-von Kármán number γ which characterizes the relative importance of shear and bending elasticity.

I. INTRODUCTION

The deformation of thin elastic sheets is a fundamental problem with many practical applications to different physical and biological systems that cover a wide range of characteristic sizes. Among these systems are macroscopic materials extending from thin steel plates via thin rubber films to paper sheets, mesoscopic materials like clay platelets, the membrane of biological cells and giant vesicles, but also microscopic materials like virus particles and carbon nano-tubes. In this paper, we focus on the elastic and mechanical properties of a model for icosahedral virus capsids for which — inspired by recent experiments with an Atomic Force Microscope (AFM) — we have studied the response to an applied uni-directional force exerted by a small colloidal particle [1].

Historically, the study of thin elastic sheets dates back to the early work of Föppl [2] and von-Kármán [3]. In the Föppl-von Kármán formalism, a thin shell of a three-dimensional homogeneous elastic material with a three-dimensional Young modulus Y , Poisson ratio ν and thickness h can be described by a mathematical surface (of zero thickness) with a two-dimensional Young modulus K_0 and a bending rigidity κ [4]. The equations that describe the mechanical equilibrium are the von-Kármán equations. For most geometries and boundary conditions a general solution of these equations is not available; therefore, one is handed over to a numerical solution of the problem. Our strategy is to solve the elastic problem using classical molecular-dynamics computer simulations.

In the remainder of this section we briefly outline the biophysical system under study. In the next section, we give a precise description of the model and the simulation method that we use, and finally in Sec. 3 we discuss some of the key results.

A virus is a tightly packaged amount of genetic material that is able to replicate in a biological cell. The genome of a virus is contained in a protective cage known as the viral

capsid. A viral capsid has a remarkably regular structure and is built up from a fixed number of copies of a single or a few kinds of capsid protein. Its geometry is that of an icosahedron or a helical cylinder, but more complex structures also exist [5]. While the in-vivo assembly of an infectious virus from its constituents is widely recognized as the paradigm for self-assembly in biology, the physical principles that underlie the structure, genome encapsulation, assembly, as well as the mechanical and transport properties of viruses remain poorly understood [6]. Many kinds of virus have been reconstituted from their components in vitro [5]. Under the right conditions of temperature, ionic strength and acidity, viral coat proteins self-assemble into virus-like particles, even in the absence of genome or in the presence of foreign genome or of a generic polyelectrolyte. Size and shape of the assemblies in those cases need not be identical to that of the native virus. This has led to the recognition that mass action drives viral assembly, that hydrophobic interactions between the coat proteins must be responsible for it, and that the electrostatic interaction between the genome and the coat proteins contributes to the viral structure and stability [5, 6]. It is therefore reasonable to explore the underlying physical principles of a virus particle without explicitly considering its biochemistry in full atomistic detail [7, 8]. For instance, the mechanical response of a viral capsid to a perturbation (either through a spontaneous fluctuation or by deliberate indentation, e.g., by means of an Atomic Force Microscope) seems very well described by continuum elasticity theory [9, 10] although it is not entirely evident why this should be the case.

Here we discuss the mechanical properties of viruses with an underlying icosahedral symmetry, which implies spherical or icosahedral capsid shapes. The origin of the stability of this shape lies in the fact that any regular triangulation of a sphere requires an excess of at least 12 five-fold disclinations. Caspar and Klug [11] showed that the organization of proteins in the viral shell is such that a few protein subunits form pentavalent and hexavalent morphological units that organize into an icosahedral shell. This shell can be characterized by two numbers p and q , which define the triangulation number or T -number of the virus, with $T = p^2 + q^2 + pq$. The number of vertices N of the triangulation then is $N = 10 T + 2$, the number of triangles is $N_T = 20 T$, and the number of protein sub-units is $3 N_T = 60 T$. For most viruses the number of subunits is rather small, so that consequently T and N_T are also small. The mechanical stability of these viruses is a direct consequence of the interactions between sub-units. These interactions are on the order of 100-400 kJ/mole which amounts to several tens of $k_B T$ per protein-protein bond. For DNA viruses, the magnitude of this binding energy has an obvious origin: the genetic material is tightly packed, resulting in a large internal pressure which drives the injection of genetic material during infection [12, 13]. For other viruses the mechanical requirements are not so clearly understood yet. Recent experiments have shown that for some viruses the thickness of the protein shell and consequently the elastic properties of the shell change during virus maturation [10, 14] and this might be relevant for virus entry in the cell.

All this suggests that the elastic properties of viral capsids play an important biophysical role. We therefore investigated the mechanical properties for a simple elastic model that, in contrast to recent finite-element calculations, correctly takes into account the geometric structure of the viral capsids. We performed a simulation study of virus indentation in a set-up very similar to the AFM experiments of Ref. [9]. This approach allows

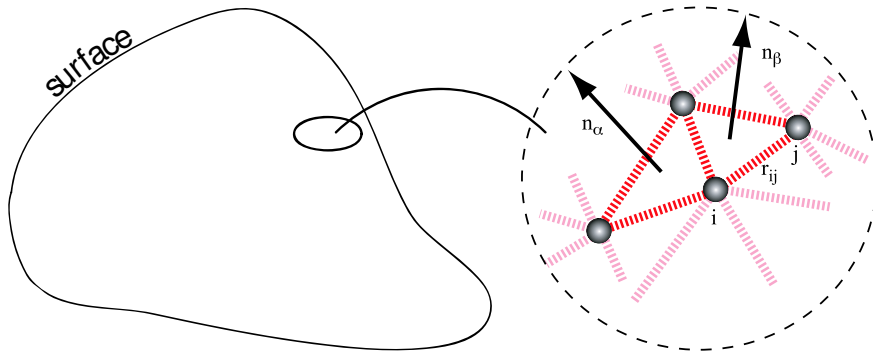


FIG. 1: Illustration of the triangulated-surface model. On the right a small portion of the surface is magnified and indicates the organization of nodes in a triangular lattice. The nodes are permanently connected by Hookean springs (Eq. 1). The bending potential is introduced via the scalar product of normal vectors on adjacent triangles (Eq. 2).

for a direct investigation of the effect of various parameters — like bending rigidity, Young modulus, capsid radius, ‘tip’ radius of the AFM, and capsid orientation — on the shape of force-deformation curves. We used a triangulated-surface model, where the number of vertices that is used to discretize the surface can be varied easily. This allows for a detailed analysis of finite-size effects; in the limit of a large number of nodes, the results should approach or become equivalent to the (unknown) solutions of continuum elasticity theory. Our results are important to properly interpret experimental force-deformation curves.

II. MODEL & METHOD

We model our icosahedral viruses using a coarse-grained triangulated-surface model. In this model, the surface is represented by discrete points that are arranged in a regular triangular lattice with fixed connectivity. Nearest-neighbor lattice points are connected by Hookean springs with spring constant k , which gives rise to a total stretching energy

$$V_s = \frac{k}{2} \sum_{\langle i,j \rangle}^N (|\mathbf{r}_i - \mathbf{r}_j| - r_0)^2. \quad (1)$$

The finite thickness of thin material shells gives rise to a resistance to bending that we model using a bending potential

$$V_b = \lambda \sum_{\langle \alpha, \beta \rangle} (1 - \mathbf{n}_\alpha \cdot \mathbf{n}_\beta). \quad (2)$$

The triangulated-surface model is illustrated in Fig. 1. In order to connect with properties of real materials, the potential parameters k and λ need to be related to the macroscopic elastic constants.

It was shown by Seung and Nelson [15] that the spring constant k can be related to the two-dimensional Young modulus via $K_0 = 2k/\sqrt{3}$, while λ is related to the bending

rigidity via $\kappa = \sqrt{3}\lambda/2$. In turn, when homogeneous shell of thickness h with Poisson ratio ν is assumed, the two-dimensional Young modulus and the bending rigidity are related to the three-dimensional elastic parameters via $K_0 = Yh$ and $\kappa = Yh^3/12(1-\nu^2)$. The ratio between bending and stretching energies is characterized by the Föppl-von Kármán number $\gamma = K_0R^2/\kappa$, where R is a characteristic length scale of the system. For the viruses we take $R = R_v$, the average radius of a virus. In general, for large γ the equilibrium shape is dominated by stretching energy, giving rise to faceted viruses, while for small γ bending contributions are important and the viruses are predominantly round in shape. In case the protein shell of viral capsids were characterized by a universal ratio K_0/κ , as argued in Ref. [7], this would imply that small viruses are round while large viruses are increasingly faceted in shape.

In Fig. 2 the simulation set-up is sketched. An icosahedron of N_T triangles is positioned with one of the faces on a supporting substrate. Then a sphere with radius R_s , initially positioned centrally on top of the virus, is moved downwards at a constant rate. This rate is chosen small enough that the deformation propagates almost instantaneous through the material. The dimensionless force $F/\sqrt{K_0\kappa}$ on the sphere is measured as a function of the dimensionless distance between sphere and substrate ($1 - \Delta z/2R_v$).

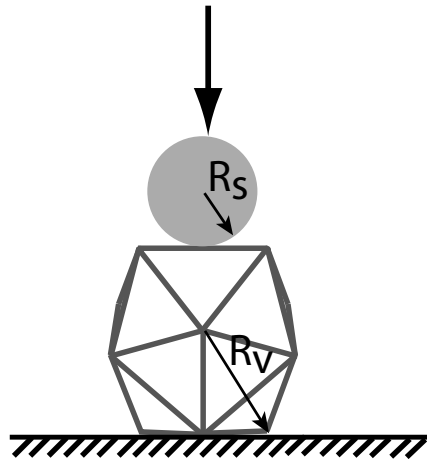


FIG. 2: Schematic illustration of the virus deformation set-up. A virus is positioned on one of its face on the substrate. A small sphere with diameter $R_s = 3r_0$ is moved downwards at a constant rate. The force on the sphere is monitored as a function of the distance between the sphere and the substrate.

III. RESULTS

We measured force-deformation curves for a large number of parameters. In Fig. 3, we show force-deformation curves for several virus shells that differ in triangulation number and in Föppl-von Kármán number. For small γ , the data with increasing T -number quickly converge to an almost linear behavior up to large compressions. For large γ , this convergence is much slower. For the smallest triangulation number of $T = 1$, a jump in the

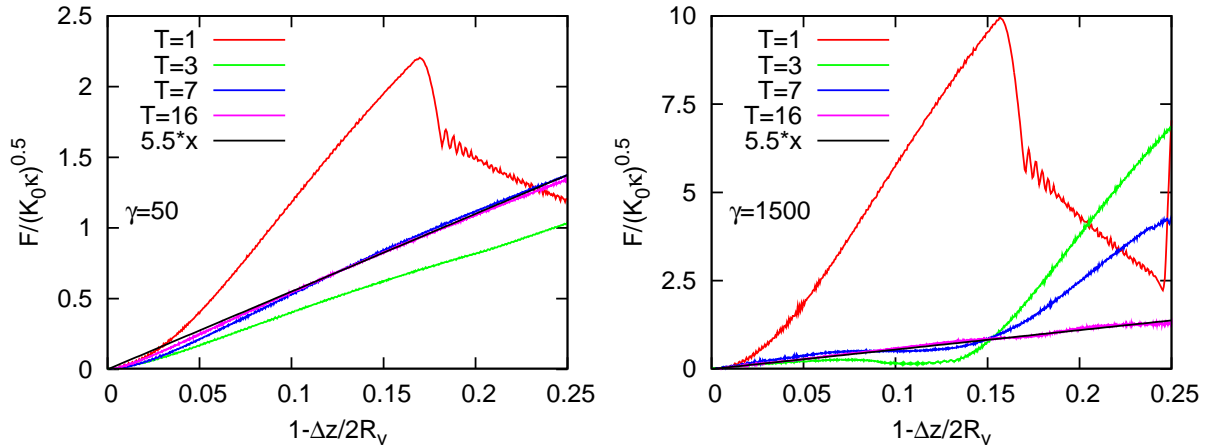


FIG. 3: Force deformation curves for the case that $R_s = 3r_0$. On the left, results for $\gamma = 50$, on the right for $\gamma = 1500$.

curve is visible, which correspond to *buckling event*, i.e. a sudden rearrangement leads to an instantaneous drop in the force on the sphere. Such buckling events are frequently observed also for large T in the case of large γ [1].

For small enough deformations all curves follow a universal scaling relation,

$$\frac{FR_v}{\kappa\sqrt{\gamma}} = C \left(1 - \frac{\Delta z}{2R_v}\right) \quad (3)$$

where F is the force the capsid exerts on the sphere and $\Delta z = z_{sphere} - z_{plate} - R_s$ is the vertical deformation. The scaling factor $R_v/\kappa\sqrt{\gamma} = 1/\sqrt{K_0\kappa}$ is the same as was found for the scaling of the buckling force of spherical shells [4] and of stretching ridges in thin elastic sheets [16]. For large γ , the initial slope of the buckling curve can be described by the same scaling relation (*i.e.* with the same value of C) while for larger compressions a second linear regime is observed with a different (larger) effective spring constant, compare Fig. 3. The details of these two regimes are discussed in Ref. [1].

For both small and large γ , the initial deformation corresponds to a *local* deformation of the surface by the tip. For increasing deformation the response becomes more and more non-local. In Fig. 4 the generic deformation pathway, as found for all simulations with this geometry, is illustrated for a one particular system. From left to right configurations at different instants of time are shown. Figure 4 bottom shows the corresponding deformations. We find that upon compression the top face deforms first, followed by an inwards flip of one of the corners of the top face. This 'flip-in' corresponds to a buckling event. Further compression of the virus leads to a cascade of smaller and much more difficult to interpret buckling events.

In recent experiments [9, 10, 17] force-deformation curves were measured for several different viruses. These data have been analyzed and interpreted so far using finite-element methods for spherical solid shells. Our results show how more precise information can be extracted from such experiments.

Finally, we want to mention that for very large Föppl-von Kármán numbers, a large number of small buckling events can be observed in the simulations, which resembles crumpling of a paper sheet. Indeed, the same model described above has been used to

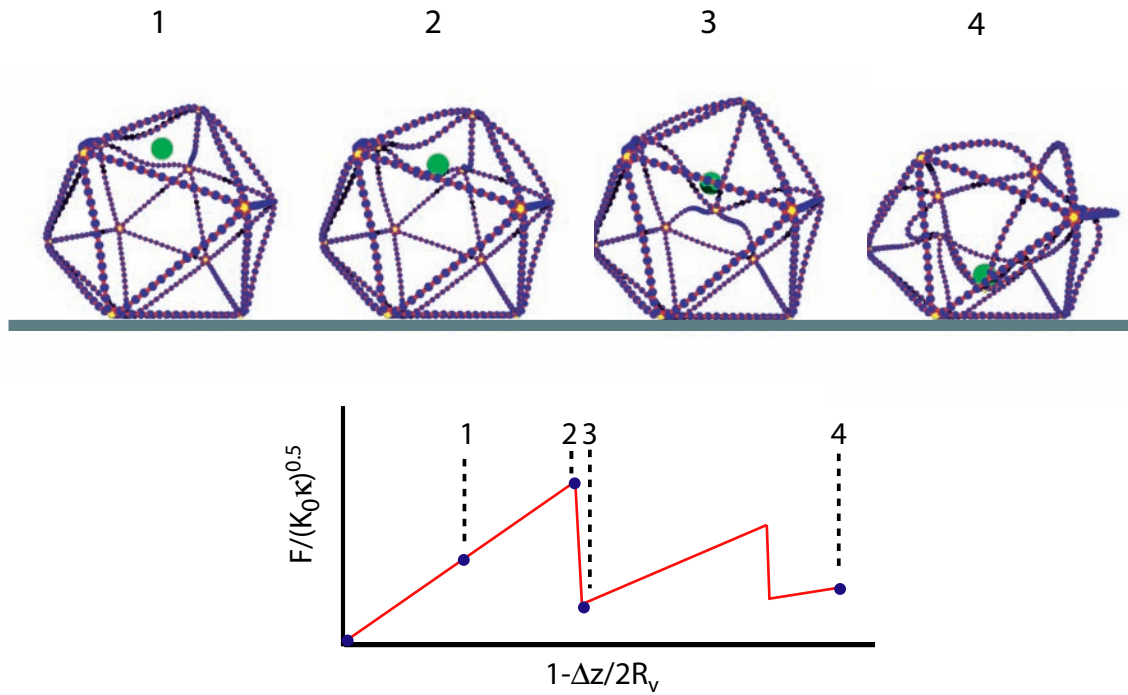


FIG. 4: Schematic illustration of the deformation pathway. Top: sequence of configurations corresponding to the deformations indicated by the numbers in the schematic deformation curve in the lower figure. ‘1’ corresponds to a small deformation, ‘2’ is the situation just before buckling (maximum stress), ‘3’ in the buckled state, and ‘4’ indicates the final state (after more than one buckling event). For clarity only the vertices that are connecting the ridges are shown.

study the intriguing pattern of folds which appears on crumpled sheets [18].

Acknowledgments: Valuable discussions with D.R Nelson, W. Gelbart and P. van der Schoot are gratefully acknowledged.

-
- [1] G. A. Vliegenthart and G. Gompper. Mechanical deformation of spherical viruses with icosahedral symmetry. *Biophys. J.* **91**, 834–841 (2006).
- [2] A. Föppl. *Vorlesungen über Technische Mechanik*, volume 5. B. G. Turner: Leipzig, Berlin (1907).
- [3] Th. von Kármán. *Collected works*. Butterworths: London (1956).
- [4] L. D. Landau and E. M. Lifshitz. *Theory of elasticity*. Butterworth-Heinemann (1986).
- [5] W. Chiu, R. M. Burnett, and R. L. Carcea, editors. *Structural biology of viruses*. Oxford University Press (1997).
- [6] R. Holland Chend and L. Hammar, editors. *Conformational proteomics of macromolecular architecture*. World Scientific: New Jersey (2004).
- [7] J. Lidmar, L. Mirny, and D. R. Nelson. Virus shapes and buckling transitions in spherical shells. *Phys. Rev. E* **68**, 051910 (2003).
- [8] R. Zandi, D. Reguera, R. F. Bruinsma, W. M. Gelbart, and J. Rudnick. Origin of icosahedral symmetry in viruses. *Proc. Natl. Acad. Sci. U.S.A.* **101**, 15556–15560 (2004).
- [9] I. L. Ivanovska, P. J. de Pablo, B. Ibarra, G. Sgalari, F. C. MacKintosh, J. L. Carrascosa, C. F. Schmidt, and G. J. L. Wuite. Bacteriophage capsids: Tough nanoshells with complex elastic properties. *Proc. Natl. Acad. Sci. U.S.A.* **101**, 7600–7605 (2004).
- [10] N. Kol, M. Gladnikoff, D. Barlam, R. Z. Shneck, A. Rein, and I. Rousso. Mechanical properties of murine leukemia virus particles: Effect of maturation. *Biophys. J.* **91**, 767–774 (2006).
- [11] D. L. D. Caspar and A. Klug. Physical principles in the construction of regular viruses. *Cold Spring Harbor Symp. on Quant. Biol.* **27**, 1–50 (1962).
- [12] A. Evilevitch, L. Lavelle, C. M. Knobler, E. Raspaud, and W. M. Gelbart. Osmotic pressure inhibition of DNA ejection from phage. *Proc. Natl. Acad. Sci. U.S.A.* **100**, 9292 (2003).
- [13] D. E. Smith, S. J. Tans, S. B. Smith, S. Grimes, D. L. Anderson, and C. Bustamante. The bacteriophage straight $\phi 29$ portal motor can package DNA against a large internal force. *Nature* **413**, 748–752 (2001).
- [14] W. R. Wikoff, J. F. Conway, J. Tang, K. K. Lee, L. Gan, N. Cheng, R. L. Duda, R. W. Hendrix, A. C. Steven, and J. E. Johnson. Time-resolved molecular dynamics of bacteriophage HK97 capsid maturation interpreted by electron cryo-microscopy and x-ray crystallography. *J. Struct. Biol.* **153**, 300–306 (2006).
- [15] H. S. Seung and D. R. Nelson. Defects in flexible membranes with crystalline order. *Phys. Rev. A* **38**, 1005–1018 (1988).
- [16] B. A. DiDonna and T. A. Witten. Anomalous strength of membranes with elastic ridges. *Phys. Rev. Lett.* **87**, 206105 (2001).
- [17] J. P. Michel, I. L. Ivanovska, M. M. Gibbons, W. S. Klug, C. M. Knobler and G. J. L. Wuite, and C. F. Schmidt. Nanoindentation studies of full and empty viral capsids and the effects of capsid protein mutations on elasticity and strength. *Proc. Natl. Acad. Sci. U.S.A.* **103**, 6184–6189 (2006).
- [18] G. A. Vliegenthart and G. Gompper. Forced crumpling of self-avoiding sheets. *Nature Materials* **5**, 216–221 (2006).

Membrane fluctuations driven by actin and myosin: waves and quantized division

Nir S. Gov¹, Roie Shlomovitz¹

¹Weizmann Institute of Science, PO Box 26, 76100 Rehovot, Israel

We present a model which couples the membrane with the protrusive forces of actin polymerization and contractile forces of molecular motors, such as myosin. The actin polymerization at the membrane is activated by freely diffusing membrane proteins, which may have a distinct spontaneous curvature. Molecular motors are recruited to the polymerizing actin filaments, from a constant reservoir, and produce a contractile force. All the forces and variables are treated in the linear limit, which allows us to derive analytic solutions. Our results show that for concave membrane proteins the myosin activity gives rise to propagating membrane waves similar to those observed on different cells. For convex membrane proteins the myosin activity gives rise to an unstable contraction, which yields a length-“quantization” of the mitosis process.

Active Transport in Disordered Microtubule Networks

Rony Granek

Department of Biotechnology Engineering, Ben Gurion University of the Negev, PO Box 653, 84105 Beer-Sheva, Israel

The motion of small cargo particles that are carried by microtubule associated motor proteins in disordered and partially disordered microtubule networks is investigated. Different network topologies in two and three dimensions are considered, one of which has been recently studied experimentally in vitro by M. Elbaum and coworkers. A generalization of the random velocity model is used to calculate the mean square displacement of the cargo particle. We find that all cases fall into the class of enhanced diffusion, that is sensitive to both the dimensionality and the topology of the network. Yet, in three dimension the motion is very close to simple diffusion. When the thermal diffusion in the bulk solution is included, no change in the asymptotic time behavior is found, as expected, but the prefactors are sensitive to the physical parameters of the system.

Vibrations in Proteins: Fractons and Dynamics Detected by Single Molecule Experiments

Rony Granek¹, Josef Klafter¹

¹*Department of Biotechnology Engineering, Ben Gurion University of the Negev, PO Box 653, 84105 Beer-Sheva, Israel*

The internal dynamics of proteins has been recently intensively studied in single molecule experiments using electron or energy transfer reactions combined with fluorescence spectroscopy. These experiments monitor the evolution in time of the distance between two associated groups on the protein from which the time autocorrelation function of this distance is deduced. Experiments from the group of X.S. Xie from Harvard show anomalous relaxation of the autocorrelation function over long periods of time. The motivation behind these experiments has been to understand the versatile biological function of protein, e.g. as enzymes. The hypothesis is that for proper protein function there is need for large internal motion that nevertheless is not changing the protein specific folding configuration nor it is inducing its unfolding.

We have advanced a theory that can explain the results of these experiments and, in addition, give a physical explanation for the major motional ability of natural folded (native) proteins (Phys. Rev. Lett. 95, 098106, (2005)). The theory is based on the description of folded proteins as fractal objects. Fractals fill up the 3-dimensional space only partially by making a structure that is „self-similar“ when one is looking at different length scales. This description has its foundations in computational analyses of known folding configurations of many different proteins and also in direct measurements. One of the main outcomes of this description is given as a generalized „Landau-Peierls instability“ that results from studying vibrations of a fractal. This effect shows that as long as the spectral dimension – that controls the change of the density of normal modes with frequency – is smaller than 2, the amplitude of the vibrations within the protein increases with increasing number of amino acids as a power-law that depends on the spectral dimension. This property enables the protein to achieve maximum vibrations without inducing unfolding. This is true so long as the spectral dimension of a given protein is such that the amplitude of the vibrations is not too large, which is consistent with computational analyses.

We calculated the autocorrelation function of the distance between two „points“ on a fractal that models a thermally vibrating protein. Using fractons, the vibrational normal modes of a fractal, they have shown that this correlation function decays anomalously, starting as a nearly stretched exponential decay and chan-

ging to an algebraic decay at long times, as observed in experiment. We conclude that this feature of the autocorrelation function is universal and not linked to the specific protein on which it is measured, nor it is dependent on the specific pair of groups (points) whose inter-distance motion is being detected. We now continue in this research direction in order to elucidate the relation between the fractal properties of folded proteins and their biological function.

Rewiring the T cell signaling network using solid-state nanostructures

Jay T. Groves

Department of Chemistry, University of California, Berkeley CA 94720

The hardware for cell signaling networks consists of cascades of chemical reactions. In recent times, it has become apparent that there are many situations in which chemically identical systems exhibit distinctively different behavior, in a seeming defiance of the laws of chemistry. On closer inspection, key differences in such cases can be found in the spatial organization of the molecules. We have developed a strategy, based on solid-state nanofabrication, to induce controlled spatial rearrangements of molecules in otherwise chemically identical living cells. These spatial mutations allow precise studies of the role of spatial organization in the function of living chemical reaction networks. We have recently applied this strategy to the study of signaling in live T cells, and have discovered a novel mechanism by which the cytoskeleton regulates signaling through the T cell receptor.

Thousands of membrane associated receptors and signaling molecules transduce signals between cells. In many cases, properties of individual binding events have proven insufficient to account for the remarkable behavior exhibited by these proteins in the cellular context. Collective protein-protein interactions and clustering on molecular length scales have been widely implicated in signal transduction. More recently, coordinated rearrangement of cell membrane receptors into distinctive patterns is emerging as a broadly significant theme of intercellular signaling. Hallmark examples are provided by the immunological synapses, which over the last few years have been discovered at junctions between a variety of immune cells and their respective target cells. Spatial patterns of proteins within the junction develop as populations of receptors on one cell membrane engage their cognate ligands on the apposed cell membrane. The emergent patterns can be microns in extent, thus transcending direct protein-protein contact interactions, and exhibit strong correlations with the ensuing intracellular signaling and effector functions.

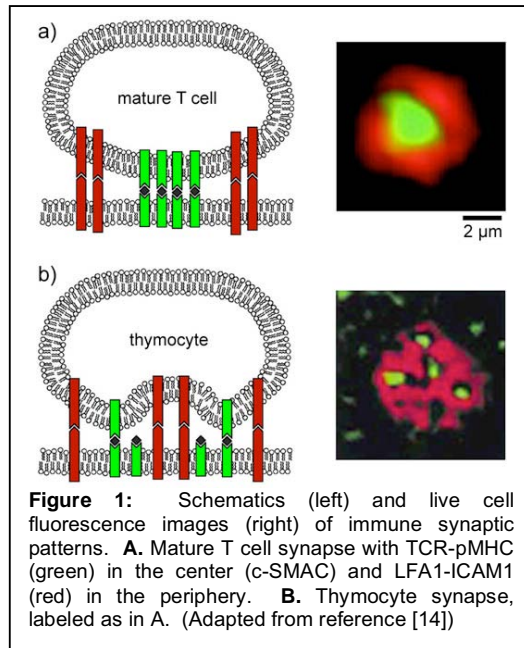
A critical role of the immune system is to identify and destroy those cells that have become infected by a pathogen or have entered into some other form of aberrant life cycle. Two classes of immune cells that perform this surveillance are T lymphocytes (T cells) and natural killer (NK) cells. T cells are the front line of the adaptive immune system and their activation primarily occurs via interaction of T cell receptors (TCRs) on the T cell with major

histocompatibility complex proteins (MHC) displaying peptide fragments on the surface of antigen presenting cells (APCs). Based on the nature of these interactions, a variety of signals can be transduced.

Both T cells and NK cells execute their surveillance processes by formation of an immunological synapse with the target cell[1-7]. A variety of recent observations have revealed precisely organized and dynamic patterns of receptors and signaling molecules within the synapse[8-13] (Figure 1)[14]. Moreover, the micron-scale geometrical configuration of these proteins exhibits a functional correlation with signaling activity. Ultimately, an elaborate assembly of co-stimulatory, adhesion, ubiquitinating, and other signaling molecules[15-19] along with cytoskeletal attachments [20-23] and lipid rafts[24-27] all become organized within immunological synapses.

Multiple functions for the geometric pattern of molecules in the synapse have been proposed[28-30]. Collectively, these ideas frame the immunological synapse as a complex signal transduction system in which multiple regulatory couplings are mediated via spatial organization. However, direct establishment of causal relationships between changes in the synaptic pattern, ligand quality and dosage, and altered signaling remain elusive.

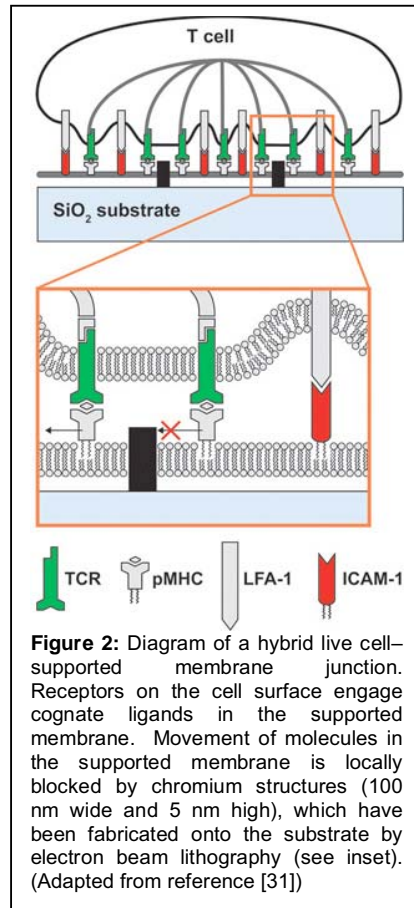
In order to explore the mechanisms of immunological synapse formation and the connectivity between spatial organization and signal regulation at intercellular junctions, we have developed an experimental platform that enables direct manipulation of synaptic patterns in living T cells[31]. A supported membrane, consisting of a continuous and fluid lipid bilayer coating a solid substrate[32], can be used to create an artificial APC surface[33]. In the case of T cells, inclusion of glycosylphosphatidylinositol (GPI) – linked forms of MHC and ICAM1 into the supported membrane is sufficient to enable immunological synapse formation between a living T cell



and the synthetic supported membrane[9]. This hybrid live cell – supported membrane synapse configuration is illustrated schematically in Figure 2[31].

A critical characteristic of supported membranes is their fluidity. A single bilayer membrane uniformly coats the surface, firmly trapped by van der Waals adhesion forces, but remaining separated from the underlying substrate by a ~1 nm thick layer of hydration water. This water layer prevents membrane components from becoming directly adsorbed on the solid substrate, enabling unconstrained rotational and translational mobility of lipids and membrane-linked proteins within the plane of the membrane. On molecular length scales, the fluid membrane environment allows assembly of multi-protein complexes. Over larger length scales, reaction-diffusion and transport processes can produce macroscopic composition patterns, such as occur during assembly of the immunological synapse. Fluidity is a unique property of supported membranes that distinguishes them from solid and polymeric substrates, which cannot afford such a range of motions. Fluid movement within the membrane, however, can be precisely controlled by fabricating geometrically-defined patterns of solid-state structures on the substrate (Figure 2, inset)[34]. Using a series of substrate-imposed constraint patterns to guide molecular motion in the supported membrane, a variety of alternatively patterned synapses between living T cells and supported membranes can be induced.

Silica substrates displaying various configurations of chromium lines (100 nm wide and 5 nm high) were fabricated by electron-beam lithography. Supported membranes, containing GPI-linked pMHC and ICAM1, were assembled on these prefabricated substrates by vesicle fusion. The chromium creates barriers that restrict the motion of lipids and proteins within the otherwise fluid and homogeneous supported membrane. This patterned



substrate forms the bottom face of a temperature-controlled flow cell, into which cells are injected. Naïve T cells from first generation AND x B10.Br mouse spleens were stimulated *in vitro* and expanded to blasts prior to use in synapse formation experiments. TCRs on these T cells recognize moth cytochrome c (MCC) 88-103 peptide (ANERADLIAYLKQATK) bound to the murine MHC class II molecule I-E^k (pMHC) in the supported membrane. Control experiments using a null peptide (T102E) show no response, confirming that the synapse formation and signaling activity are antigen specific and that TCR clustering does not originate from the chromium patterns. As receptors on the T cell surface engage their cognate ligands in the underlying supported membrane, they become subject to the geometrical pattern of mobility restrictions imposed by the substrate. In this way, substrate patterns can influence the transport of proteins and signaling machinery within the living cell. Other than the underlying freedom-of-motion constraint, the initial distributions of proteins in the supported membrane are homogeneous and exhibit free lateral diffusion. Spatial patterns within fully formed synapses are driven entirely by the T cell. The patterns differ from the wild type concentric rings of the c-SMAC and p-SMAC as a result of the mechanisms by which the T cell drives protein rearrangements and the way different geometric and mobility constraints on the substrate frustrate these processes.

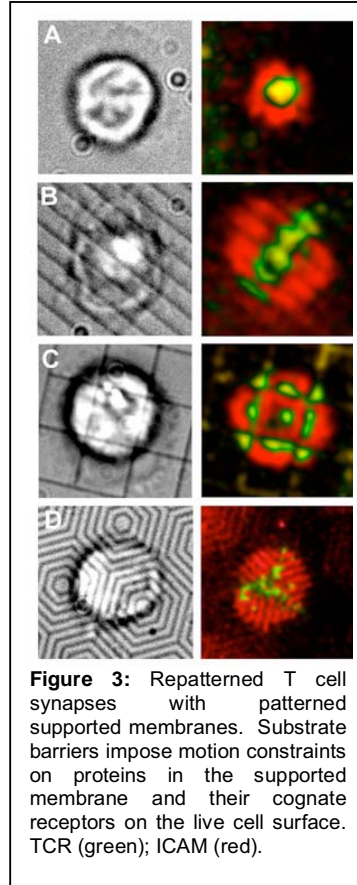
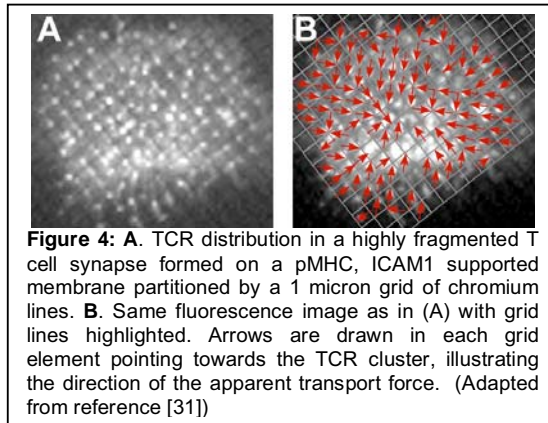


Figure 3: Repatterned T cell synapses with patterned supported membranes. Substrate barriers impose motion constraints on proteins in the supported membrane and their cognate receptors on the live cell surface. TCR (green); ICAM (red).

A series of four synaptic patterns, formed under different substrate constraint geometries, are pictured in Figure 3. Unrestricted synapses form the characteristic c-SMAC (3A). Constraint patterns consisting of arrays of parallel lines, such as shown in Figure 3B, restrict protein mobility in one dimension and skew the synaptic pattern from a circular to a rectangular shape in which a central band of TCR-pMHC is flanked by two bands of LFA1-ICAM1. Multifocal synapses form when grid constraint patterns create an array of isolated membrane corrals (3C). More elaborate constraint patterns, such as the mosaic of concentric hexagonal barriers illustrated in

Figure 3D, can also be used. T cells were observed to form synapses under all of the constraint patterns studied, providing a diverse collection of alternative synaptic patterns.

The initial distribution of TCR on the T cell surface is believed to be homogeneous. In our experiments, we observed T cell contact with the supported membrane, the nucleation of TCR microclusters, and then the organization of the microclusters into a c-SMAC. This process is guided by chromium barriers on the silica substrate. Using total internal reflection fluorescence microscopy, the transport patterns of individual TCR microclusters and their interactions with the substrate-imposed constraint grids can be resolved.



Analysis of the final patterns, as well as their intermediate stages during formation, can be used to reveal the underlying mechanisms of synapse formation. A representative image of a highly fragmented T cell synapse, consisting of more than 100 micro-synaptic clusters of TCR-pMHC complexes, formed on a 1 μm grid of constraint barriers is illustrated in Figure 4[31]. Several mechanistic aspects of synapse formation can be discerned from this image. The microclusters remain stable and trapped for more than 30 min, in spite of the rapid TCR-pMHC off rate ($\sim 0.01\text{-}0.1\text{ s}^{-1}$ [35]). Since TCR motion can presumably only be constrained by the grid through engagement with pMHC, the long-term stability of these microclusters indicates that multiple TCR are moving as a unit. Otherwise, individual TCR could percolate over the narrow barriers during momentary disengagements from pMHC. The position of each TCR-pMHC microcluster within its corral reveals the direction of the transport force, and can be used to compile a comprehensive transport map over the entire synaptic interface. In Figure 4B, the underlying constraint pattern is highlighted with gray lines and an arrow has been drawn in each corral, pointing towards the position of the TCR-pMHC microcluster. The clusters are generally pulled to the corner of the corral nearest the center of the synapse; highly consistent radial coordination of the microcluster positions is almost always observed on grid constraint patterns. We have developed an image analysis strategy for quantification of this coordinated positional information. The methodology provides a unique observation of static force. Typically one TCR-pMHC cluster is observed per

corral for the 1, 2, and 5 μm square grids studied. This observation suggests that TCR clustering occurs only after pMHC engagement. If TCR were substantially preclustered, one would expect a stochastic distribution of microclusters within the corrals rather than the even distributions we generally observe. Collectively, this set of observations illustrates a three step process by which the mature T cell synapse forms: *i*) TCR engage pMHC; *ii*) TCR-pMHC assemble into microclusters that are segregated from the adhesion molecules (with differing topographical size); *iii*) microclusters are transported to the forming c-SMAC in a directed manner, presumably by signaling-induced cytoskeletal motion and membrane forces.

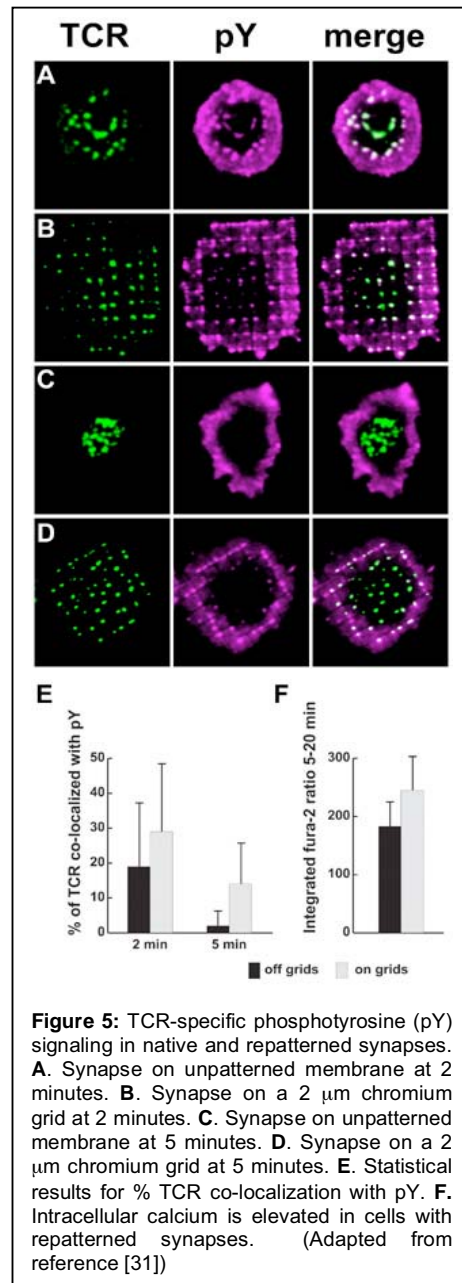
Each T cell receptor is a multi-unit protein consisting of an $\alpha\beta$ heterodimer associated with a CD3 complex, which has on its cytoplasmic side a number of immunoreceptor tyrosine-based activation motifs (ITAMs). The ITAMs contain several locations that are phosphorylated by the kinase Lck and serve as origins of TCR-specific signaling. The cytoplasmic distribution of phosphorylated tyrosine (pY) residues serves as a measure of the signaling strength, and can be monitored by immunofluorescent staining with the anti-pY antibody 4G10. Cells were incubated over the supported membranes for 2 and 5 minute periods, they were then fixed and stained for pY.

A distinctive sequence of TCR spatial organization and pY signaling is observed during early stages of synapse formation. Shortly after the first contact between the T cell and the APC surface, microclusters of TCR form and are spatially co-localized with regions of relatively increased pY signaling. Representative images of TCR (green) and pY (purple) for synapses forming on unrestricted supported membranes and supported membranes constrained by 2 μm grids of diffusion barriers are illustrated in Figure 5[31]. Images in 5A and 5B were taken two minutes after the T cells contacted the APC surface and are illustrative of the TCR signaling activity at this nascent stage of synapse formation. In addition to the direct co-localization of TCR microclusters with regions of high pY signaling, which can be seen clearly in the central region of the nascent synapse, a diffuse ring of pY signaling appears in the periphery. A portion of this does not co-localize with TCR microclusters, specifically, and may represent integrin-related signaling, which is also detected by the anti-pY antibody, or signaling from TCR microclusters. However, regions of relatively higher pY signaling, over this diffuse background, can be seen co-localized with the TCR microclusters. In general, TCR specific signaling activity is observed for all TCR microclusters at the 2 minute time point, for both constrained and unconstrained synapses alike.

Five minutes after contact, a well resolved c-SMAC is seen to form in the constraint free case. This is the native T cell synaptic pattern. As seen in Figure 5C, no signaling activity is detected from the TCRs, all of which are

concentrated in the c-SMAC. The diffuse ring of non-TCR signaling is still observed in the periphery. In striking contrast to the consistent shutdown of TCR signaling seen in the native (unrestricted) synaptic pattern, the prevention of TCR transport to the forming c-SMAC prolongs TCR specific signaling. This can be seen clearly in Figure 5D, in which bright regions of pY signaling above the diffuse background are co-localized with the trapped peripheral TCR microclusters. The enhanced signaling, however, is restricted to the periphery. TCR clusters trapped in more central regions of the synapse no longer signal.

Image analysis can be used to compute the percentage of TCR in each cell that co-localized with regions of intense pY signaling. To quantify the TCR-specific portion of the pY signal, we compute the cross correlation between the TCR pattern and the pattern of spikes in pY signal above the local background. Results from this cross correlation analysis appear as small white spots in Figure 5 A – D, and are summarized in Figure 5E. At 2 minutes, moderately enhanced TCR co-localization with pY is seen in restricted synapses relative to the unrestricted synapses. Re-patterning effects from the diffusion barriers are already acting to prolong TCR signaling. At five minutes after contact, the contrast is unmistakable: cells forming native synapses had $2 \pm 4\%$ co-localization,



corresponding to near-total shutdown, while cells with re-patterned synapses on 2 μm grids had $14\pm 12\%$ co-localization, which visually corresponds to phosphorylation of all TCR trapped in the peripheral ring. Mechanical trapping of TCR microclusters in the synapse periphery apparently prolongs pY signaling.

Another key measure of signaling activity is the flux of intracellular Ca^{2+} induced by TCR antigen recognition, which integrates the outputs of all TCR signaling events in the synapse[36]. T cells were loaded with the ratiometric calcium-sensitive dye fura-2 and allowed to interact with pMHC-ICAM membranes. The fura-2 fluorescence emission ratio (510 nm emission with 340 nm vs. 380 nm excitation) was integrated from 5 min to 20 min in cells on and off 2- μm grids. Data from five independent experiments (totaling 49 cells on and 57 cells off grids) is plotted in Figure 5F. The integrated Ca^{2+} response was significantly higher in cells with spatially repatterned synapses as compared to those with native synaptice patterns. Thus, mechanical trapping of TCR in the synapse periphery augments early TCR associated pY levels and the elevation of cytoplasmic Ca^{2+} .

References

1. vanderMerwe, P.A. and S.J. Davis, *The immunological synapse - a multitasking system*. Science, 2002. **295**: p. 1479-1480.
2. Bromley, S.K., et al., *The immunological synapse*. Annu. Rev. Immunol., 2001. **19**: p. 375-396.
3. Dustin, M.L., et al., *Identification of self through two-dimensional chemistry and synapses*. Annu. Rev. Cell Dev. Biol, 2001. **17**: p. 133-157.
4. Krummel, M.F. and M.M. Davis, *Dynamics of the immunological synapse: finding, establishing and solidifying a connection*. Curr. Op. Immunol., 2002. **14**: p. 66-74.
5. Davis, D.M., *Assembly of the immunological synapse for T cells and NK cells*. TRENDS Immunol., 2002. **23**(7): p. 356-363.
6. Wülfing, C., et al., *Interface accumulation of receptor/ligand couples in lymphocyte activation: methods, mechanisms, and significance*. Immunol. Rev., 2002. **189**: p. 64-83.
7. McCann, F.E., et al., *Imaging immune surveillance by T cells and NK cells*. Immunol. Rev., 2002. **189**: p. 179-192.
8. Monks, C.R.F., et al., *Three-dimensional segregation of supramolecular activation clusters in T cells*. Nature, 1998. **395**: p. 82-86.
9. Grakoui, A., et al., *The immunological synapse: A molecular machine controlling T cell activation*. Science, 1999. **285**: p. 221-227.
10. Krummel, M.F., et al., *Differential Clustering of CD4 and CD3z during T-cell recognition*. Science, 2000. **289**: p. 1349-1352.
11. Lee, K.-H., et al., *T cell receptor signaling precedes immunological synapse formation*. Science, 2002. **295**: p. 1539-1542.

12. Stoll, S., et al., *Dynamic imaging of T cell-dendritic cell interactions in lymph nodes*. *Science*, 2002. **296**: p. 1873-1876.
13. Davis, D.M., et al., *The human natural killer cell immune synapse*. *Proc. Natl. Acad. Sci. USA*, 1999. **96**(26): p. 15062-15067.
14. Groves, J.T., *Molecular organization and signal transduction at intermembrane junctions*. *Angew. Chem. Int. Ed.*, 2005. **44**: p. 3524-3538.
15. Tseng, S.-Y. and M.L. Dustin, *T-cell activation: a multidimensional signaling network*. *Curr. Op. Cell Biol.*, 2002. **14**: p. 575-580.
16. Werlen, G. and E. Palmer, *The TCR signalosome: a dynamic structure with expanding complexity*. *Curr. Op. Immunol.*, 2002. **14**: p. 299-305.
17. Sims, T.N. and M.L. Dustin, *The immunological synapse: integrins take the stage*. *Immunol. Rev.*, 2002. **186**: p. 101-117.
18. Arendt, C.W., et al., *Protein kinase C-theta: signaling from the center of the T-cell synapse*. *Curr. Op. Immunol.*, 2002. **14**: p. 323-330.
19. Vyas, Y.M., H. Maniar, and B. Dupont, *Visualization of signaling pathways and cortical cytoskeleton in cytolytic and noncytolytic natural killer cell immune synapses*. *Immunol. Rev.*, 2002. **189**: p. 161-178.
20. Wülfing, C. and M.M. Davis, *A receptor/cytoskeletal movement triggered by costimulation during T cell activation*. *Science*, 1998. **282**: p. 2266-2269.
21. Dustin, M.L. and J.A. Cooper, *The immunological synapse and the actin cytoskeleton: molecular hardware for T cell signaling*. *Nature Immunology*, 2000. **1**: p. 23-29.
22. Das, V., et al., *Membrane-cytoskeleton interactions during the formation of the immunological synapse*. *Immunol. Rev.*, 2002. **189**: p. 123-135.
23. Fuller, C.L., V.L. Braciale, and L.E. Samelson, *All roads lead to actin: the intimate relationship between TCR signaling and the cytoskeleton*. *Immunol. Rev.*, 2003. **191**: p. 220-236.
24. Viola, A., et al., *T Lymphocyte costimulation mediated by reorganization of membrane microdomains*. *Science*, 1999. **283**: p. 680-682.
25. Dykstra, M., A. Cherukuri, and S.K. Pierce, *Rafts and synapses in the spatial organization of immune cell signaling receptors*. *J. Leukoc. Biol.*, 2001. **70**: p. 699-707.
26. Dustin, M.L., *Membrane domains and the immunological synapse: keeping T cells resting and ready*. *J. Clin. Invest.*, 2002. **109**: p. 155-160.
27. Pizzo, P., et al., *Physiological T cell activation starts and propagates in lipid rafts*. *Immunol. Lett.*, 2004. **91**: p. 3-9.
28. Davis, D.M. and M.L. Dustin, *What is the importance of the immunological synapse?* *TRENDS Immunol.*, 2004. **25**(6): p. 323-327.
29. Jacobelli, J., et al., *New views of the immunological synapse: variations in assembly and function*. *Curr. Opin. Immunol.*, 2004. **16**: p. 345-352.
30. Friedl, P. and J. Storim, *Diversity in immune-cell interactions: states and functions of the immunological synapse*. *TRENDS Cell Biol.*, 2004. **14**(10): p. 557-567.

31. Mossman, K.D., et al., *Altered TCR signaling from geometrically repatterned immunological synapses*. *Science*, 2005. **310**: p. 1191-1193.
32. Sackmann, E., *Supported membranes: Scientific and practical applications*. *Science*, 1996. **271**: p. 43-48.
33. Groves, J.T. and M.L. Dustin, *Supported planar bilayers in studies of immune cell adhesion and communication*. *J. Immunol. Methods*, 2003. **278**: p. 19-32.
34. Groves, J.T., N. Ulman, and S.G. Boxer, *Micropatterning fluid lipid bilayers on solid supports*. *Science*, 1997. **275**: p. 651-653.
35. Davis, M.M., et al., *Dynamics of cell surface molecules during T cell recognition*. *Annu. Rev. Biochem.*, 2003. **72**: p. 717-742.
36. Irvine, D.J., et al., *Direct observation of ligand recognition by T cells*. *Nature*, 2002. **419**: p. 845-849.

How to Coarse Grain Ion Potentials in Aqueous Solutions

Berk Hess¹, Christian Holm^{1,2}, Nico van der Vegt¹

¹Max-Planck Institute for Polymer Research, Ackermannweg 10, D-55128 Mainz, Germany, hessb@mpip-mainz.mpg.de; ²FIAS, J.W. Goethe Universität, Max-von-Laue Strasse 1, D-60438 Frankfurt/Main, Germany

ABSTRACT

We report a new strategy to parameterize effective ion-ion potentials for implicit solvent simulations of charged systems. The effective potential includes a pair term and a Coulomb term that by means of a concentration dependent dielectric permittivity takes into account multi-body effects. We demonstrate that this approach allows to accurately reproduce the solution osmotic properties and the ion coordination up to concentrations of 2.8 molar aqueous NaCl.

1. Introduction

Ions in aqueous solutions play an important role in many biological and man-made systems. The ions can be involved directly, for example, in interactions with proteins, or indirectly by screening interactions between charged molecules in solution. In both cases the behavior of the system depends strongly on the spatial distribution of the ions. To model the proper ion distribution large length scales are required, because of the long-ranged nature of electrostatic interactions. As the system sizes prohibit the use of explicitly modeled solvent molecules one has to use effective potentials that implicitly take solvation into account. For a single solute species at a fixed concentration more accurate potentials can be obtained by Boltzmann inversion of pair distributions functions. For ionic solutions, however, one can not directly invert the distributions of the three ion pairs as they are not independent. One can approximate the effective interactions between the ions with pair potentials using McMillan-Mayer theory, through reverse Monte Carlo or the hypernetted-chain approximation.[1, 2] The problems of this approach are that the potentials are not unique, for each density of interest one has to perform long simulations to obtain accurate distributions.

2. Methods

Here we describe a method that avoids the disadvantages of Boltzmann inversion by splitting the procedure into two parts.[3] We will use NaCl in aqueous solution as an example system. First we derive effective pair potentials for the three different ions pairs at high dilution. This we do by using atomistic simulations of a single ion pair in a box (3.5 nm rhombic dodecahedron) with 1000 water molecules. The effective force is determined by constraining the distance between Na⁺-Cl⁻, Na⁺-Na⁺ and Cl⁻-Cl⁻ and measuring the constraint force. To account for multi-body effects, certainly present at high ionic concentrations, a concentration dependent dielectric permittivity $\epsilon_E(c)$ is introduced in

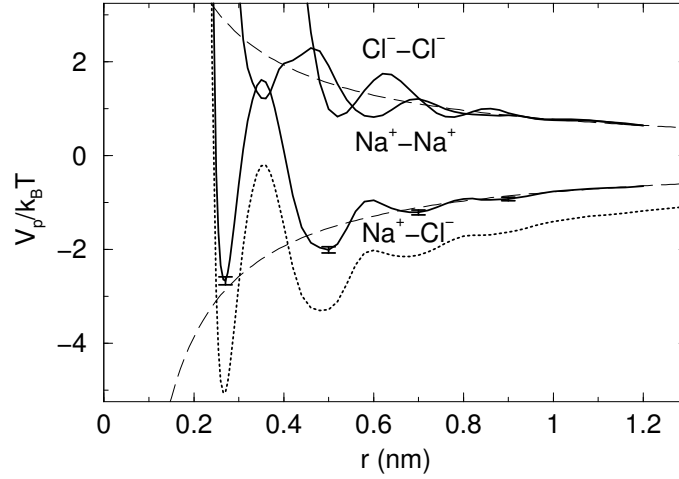


Figure 1: The effective potential for single ion pairs with the WS force-field (solid lines), $V_s(r, c)$ for $c = 2.8$ M (dotted line) and pure Coulomb curves with $\epsilon_r = 72$ (dashed lines).

a Coulomb term augmenting the long-ranged part of the effective pair potential. We demonstrate that to obtain these permittivities, in practice only a single simulation at a high salt concentration is required. We will show that the effective potential accurately reproduces the pair distribution functions of the explicit solvent simulations, as well as the experimentally measured osmotic coefficient. The latter result can also be achieved by replacing the short-ranged part of the effective potential with a simple repulsive potential. Extending this procedure to inhomogeneous systems would allow for the first time an accurate description using an implicit solvent.

We used the atomistic force-field parameterized by Weerasinghe and Smith (WS)[4], which should be used with the SPC/E water model. The electrostatic interactions are treated with the particle-mesh Ewald method (PME). We performed constrained simulations of 4 to 8 ns at 300 K for the three ion pairs for up to 56 distances ranging from 0.23 to 1.2 nm. Integrating the constraint force from $r_m = 1.2$ nm downwards gives the effective potential with respect to r_m . Here one has to correct for the entropic volume contribution of $2k_B \log(r)$, because the volume sampled by the two ions rotating around each other scales as r^2 . As beyond 1 nm the curve is very smooth we assume that the effective potential beyond is given by the Coulomb potential. The total effective potential can then be written as:

$$V_p(r) = \begin{cases} \int_{r_m}^r \left[\langle f_c \rangle_s + \frac{2k_B T}{s} \right] ds + \frac{q_1 q_2}{4\pi\epsilon_0} \left(\frac{1}{\epsilon_E(c)r} - \frac{1}{\epsilon_E(0)} \left[\frac{1}{r} - \frac{1}{r_m} \right] \right) & , r < r_m \\ \frac{q_1 q_2}{4\pi\epsilon_0 \epsilon_E(c) r} & , r \geq r_m \end{cases} \quad (1)$$

where f_c is the constraint force. To obtain the dielectric permittivity $\epsilon_E(0)$ we performed 80 ns simulations of 1000 SPC/E water molecules, which resulted in $\epsilon_E(0) = 71.9 \pm 0.6$. The effective potentials are shown in Fig. 1.

3. Implicit solvent simulations

Using the above obtained effective ion-ion potentials we performed implicit solvent simulations using a relative dielectric permittivity of $\epsilon_r = 71.9$. We have done this using PME

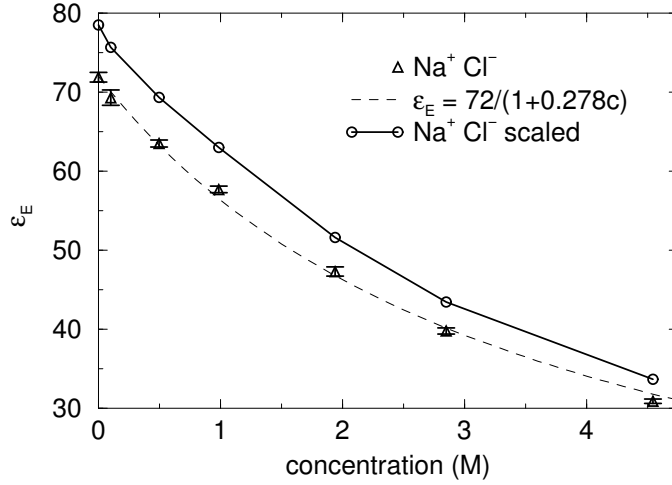


Figure 2: The NaCl concentration dependent dielectric permittivity ϵ_E for the WS force-field, a fit and ϵ_E scaled to 78.5 at zero concentration which is used for the WCA model.

for 100 ion pairs at six salt concentrations ranging from 0.1 M to 4.5 M, corresponding to 555 to 11.1 water molecules per ion pair. What one observes is that due to the absence of multi-body terms in the effective potential the $\text{Na}^+\text{-Cl}^-$ coordination is underestimated. The major multi-body effect at higher NaCl concentrations arises from electrostriction of water. When three or more ions approach each other strong local electrostatic fields suppress orientation fluctuations of water molecules. It turns out that the multi-body effects can be captured well by a concentration dependent effective dielectric permittivity $\epsilon_E(c)$, where c is the salt molarity. It is determined from a part of the dipole fluctuation of a solution by considering the contribution of the water molecules only[5]. To determine $\epsilon_E(c)$ we have performed simulations of 40 ion pairs for 50 ns in SPC/E water, the results are shown in Fig. 2. The scaling factor for the electrostatic interactions $1/\epsilon_E$ can be fitted very well with a straight line (Fig. 2). This means that to determine $\epsilon_E(c)$ in practice it suffices to simulate two small systems, one consisting of pure water and one salt solution at a high concentration.

With the correction we obtain the correct coordination up to a concentration of 2.8 M. The radial distribution functions match perfectly (Fig. 3). Only at 4.5 M we start to see an underestimation of the $\text{Na}^+\text{-Cl}^-$ coordination. Such a superposition has been demonstrated for finite concentrations before for $\text{Na}^+\text{-Na}^+$ interactions, by empirically fitting ϵ_r at each concentration to obtain the best possible overlap of the short-range potentials[6]. We have shown that this superposition also works for a NaCl solution, which contains the much stronger interacting $\text{Na}^+\text{-Cl}^-$ pairs, but more importantly that it has a physical basis in the $\epsilon_E(c)$ determined from dipole fluctuations.

We compared the 'sophisticated' effective potential with a simpler Coulomb plus a Weeks-Chandler-Andersen (WCA) potential:

$$V_s(r, c) = \begin{cases} \frac{q_1 q_2}{4 \pi \epsilon_0 \epsilon_E(c) r} + k_B T \left[4 \left(\frac{\sigma}{r} \right)^{12} - 4 \left(\frac{\sigma}{r} \right)^6 + 1 \right] & , r < 2^{\frac{1}{6}} \sigma \\ \frac{q_1 q_2}{4 \pi \epsilon_0 \epsilon_E(c) r} & , r \geq 2^{\frac{1}{6}} \sigma \end{cases} \quad (2)$$

For σ we used the WS force-field values: 0.33 nm for $\text{Na}^+\text{-Cl}^-$, 0.25 nm for $\text{Na}^+\text{-Na}^+$ and 0.44 nm for $\text{Cl}^-\text{-Cl}^-$. Note that the values for the like-charged ion pairs have little

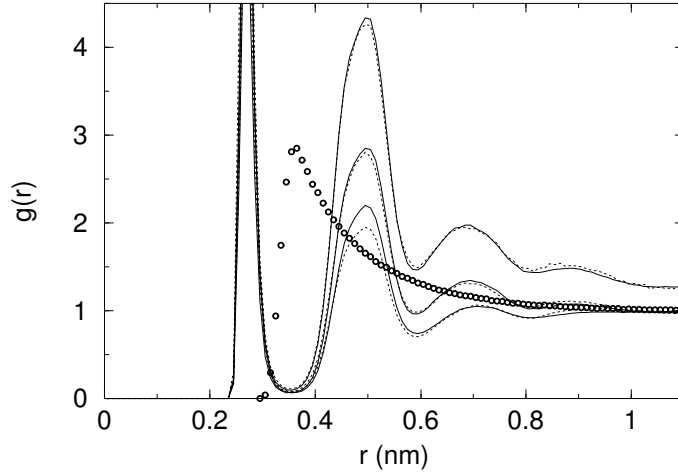


Figure 3: The $\text{Na}^+\text{-Cl}^-$ radial distribution function for the explicit solvent (solid lines) and implicit solvent (dotted lines) WS systems at concentrations of $c = 0.1, 1$ and 4.5 M, upper, middle and lower curves respectively. The circles show the WCA model at 1 M.

influence on the results. We simulated this model under the same conditions as the effective potential simulations, but with the dielectric permittivity scaled using reference value of 78.5 at infinite dilution (Fig. 2). Although the radial distribution functions are completely different (Fig. 3), the $\text{Na}^+\text{-Cl}^-$ coordination matches the WS model perfectly up to a concentration of 1.9 M. At 2.8 M it slightly underestimates the atomistic values. Apparently the detailed minima and maxima of the effective potential are not important for the ion coordination.

With effective potentials between ions, one can determine the osmotic pressure or osmotic coefficient, which is difficult for simulations with explicit solvent. The osmotic coefficient ϕ is defined as the pressure divided by the ideal gas pressure:

$$\phi = \frac{P}{P_{ideal}} = \frac{K - \Xi}{K} = 1 - \frac{\Xi}{K} \quad (3)$$

where K is the kinetic energy and Ξ is the virial. This quantity allows for a direct comparison of computer models with experiment. The values as a function of concentration are shown for the different models as well as experiment[7] in Fig. 4. The WS model nicely follows the experimental trend, but is slightly too low over the whole concentration range. We also tried the WS force-field in combination with the SPC water model. Due to the too low dielectric permittivity of 65.5 , the osmotic coefficient is slightly underestimated at lower concentrations and significantly overestimated at higher concentrations (results not shown). Note that if one uses a fixed dielectric permittivity the osmotic coefficient is far off at higher concentrations (Fig. 4). The WCA model is closer to the experiment, which is surprising for such a simple model. At low concentrations this improvement is due to the correction for the dielectric permittivity.

The properties of the WCA model depend, apart from $\epsilon_E(c)$, mainly on the parameter σ for $\text{Na}^+\text{-Cl}^-$, the σ for the like charged pairs has little influence as they repel each other.

4. Atomistic force field accuracy

With the same procedure we have derived effective potentials for several combinations of biomolecular force fields for Na^+ and Cl^- and four water models.[8] The ion potentials in most biomolecular force fields have been parameterized on the salt crystal and/or the

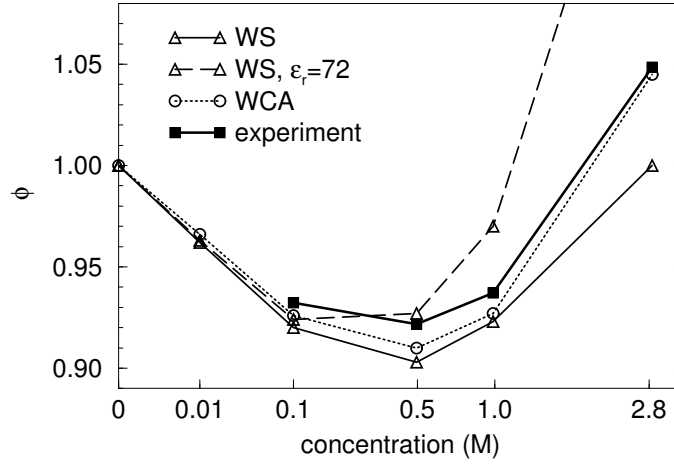


Figure 4: The osmotic coefficient as a function of the cube root of the salt concentration for the models and experiment[7] as indicated. All models use a concentration dependent dielectric permittivity, except for the $\epsilon_r = 72$ curve.

ions	water	$\epsilon_E(0)$	$\phi, c=0.1 \text{ M}$	$\phi, c=1.0 \text{ M}$	$\phi, c=2.8 \text{ M}$
AMBER	TIP3P	98	0.943	aggr.	aggr.
CHARMM	TIP3P	98	0.950	0.95	1.03
CHARMM	TIP4P-Ew	65	0.898	0.85	0.86
GROMOS	SPC	66	0.903	aggr.	aggr.
WS	SPC/E	72	0.923	0.92	1.00
WS	SPC	66	0.918	0.94	1.08
experiment		78	0.932	0.94	1.05

Table 1: The osmotic coefficient ϕ for different force field and water model combinations as well as experiment at three concentrations; aggr. indicates that the ions form aggregates. Also shown are the dielectric permittivities $\epsilon_E(0)$ for the water models.

solvation free-energy of a single ion. One can therefore not expect that such force fields reproduce the correct structure of NaCl(aq). Indeed from Tab. 1 one can see that the osmotic coefficient differ strongly between force fields as well as water models. For the AMBER and GROMOS force fields the first minimum of the effective $\text{Na}^+\text{-Cl}^-$ potential is too deep, which causes aggregation at higher concentrations. For the other force fields the first minimum is less important and the properties of the solution are mainly determined by the depth of the second minimum. Because the osmotic coefficient is very sensitive to the interactions in the solution, this procedure can be used to verify and improve atomistic force fields. A prerequisite for a good force field is that the dielectric permittivity of the water model is close to the experimental value, as the effective interactions between the ions depend strongly on this property.

5. Conclusions

We have shown that multi-body effects between solvated ions, which start playing a role already at a concentration of 0.5 M, can be captured accurately by the use of a concentration dependent dielectric permittivity $\epsilon_E(c)$. As $1/\epsilon_E$ depends linearly on the concentration, it can be determined from a single simulation of a small, concentrated salt solution,

assuming that the dielectric permittivity of the water model is known. Based on these effective potentials the ion-ion correlation functions of the explicit solvent simulations and the experimental osmotic coefficients are reproduced up to 2.8 M. Moreover, when one is not interested in spatial resolutions on the order of a few Ångströms, a WCA potential performs just as well, as the excellent agreement with the experimental osmotic coefficients shows. In addition, even the ion coordination matches the WS results up to 1.9 M. There is only one important parameter left, namely the distance of closest approach of the cation and anion, which is set by the WCA σ , and which can be determined by matching the ion coordination at a single concentration. This provides an extremely efficient way to simulate the thermodynamic properties of electrolyte solutions. For the important case of inhomogeneous systems that contain for example charged macromolecules or membranes, we suggest that the use of a local concentration dependent dielectric permittivity will enhance greatly the accuracy of large-scale implicit solvent simulations.

Acknowledgments

The authors acknowledge Kurt Kremer for helpful discussions and financial support from the DFG under grants Ho 1108/11-2 and SFB 625.

References

- [1] A. P. Lyubartsev and A. Laaksonen, Calculation of Effective Interaction Potentials from Radial Distribution Functions: A Reverse Monte Carlo Approach, *Phys. Rev. E* **52**, 3730 (1995).
- [2] A. P. Lyubartsev and S. Marčelja, Evaluation of effective ion-ion potentials in aqueous electrolytes, *Phys. Rev. E* **65**, 041202 (2002).
- [3] B. Hess, C. Holm, and N. van der Vegt, Modeling multi-body effects in ionic solutions with a concentration dependent dielectric permittivity, *Phys. Rev. Lett.* **96**, 147801 (2006).
- [4] S. Weerasinghe and P. E. Smith, A Kirkwood-Buff derived force field for sodium chloride in water, *J. Chem. Phys.* **119**, 11342 (2003).
- [5] D. Levesque, J. J. Weis, and G. N. Patey, Charged hard spheres in dipolar hard sphere solvents. A model for electrolyte solutions., *J. Chem. Phys.* **72**, 1887 (1980).
- [6] R. Kjellander, A. P. Lyubartsev, and S. Marčelja, McMillan-Mayer theory for solvent effects in inhomogeneous systems: Calculation of interaction pressure in aqueous electrical double layers, *J. Chem. Phys.* **114**, 9565 (2001).
- [7] D. G. Archer, Thermodynamic Properties of the NaCl + H₂O System II. Thermodynamic Properties of NaCl(aq), NaCl·H₂O(cr), and Phase Equilibria, *J. Phys. Chem. Ref. Data* **21**, 793 (1992).
- [8] B. Hess, C. Holm, and N. van der Vegt, Osmotic coefficients of atomistic NaCl (aq) force fields, *J. Chem. Phys.* **124**, 164509 (2006).

Microscopic simulations of macroscopic consequences: fixing the continuum and hybrid methods

Uzi Landman

School of Physics, Georgia Institute of Technology, 837 State Street, 30332-0430 Atlanta, USA

Computationally-based modeling and simulations play an increasingly important role in modern condensed matter physics, chemistry, materials science, and biology [1]. In particular, such studies, allow explorations of complex phenomena with refined resolution in space and time. Furthermore, in some occasions atomistic simulations may be regarded, and used, as numerical experiments whose analysis guides formulation of new theoretical treatments of continuum nature. To discuss and illustrate the above physical and methodological issues, we focus first on the properties of certain fluid systems under highly confined conditions, including:

* Atomistic simulations of the generation, stability, and breakup of nanojets and liquid nano structures, in vacuum as well as in ambient environments, and the development of a continuum stochastic Navier-Stokes approach that includes size-dependent fluctuations and environmental influences, thus extending the range of validity of deterministic continuum hydrodynamic formulations to the molecular scale [2].

* Nanotribological processes, simulations and modeling the atomistic origins of Amontons' law describing macroscopic frictional observations [3], layering transitions of highly confined liquids, and methods for the control of friction. In the second part of the talk we discuss hybrid methods where classical and quantum treatments are combined in order to explore efficiently the behavior of systems where the quantum part may be spatially localized, but the inclusion of an extended part of the systems, interacting with the localized quantum region, is essential. We illustrate such studies through recent investigation of hole transport and reactions of ionized DNA with water leading to mutagenesis and disease [4], and probing of the formation of surface and interior excess electron states in water clusters.

1. U. Landman, "Materials by Numbers: Computations as Tools of Discovery", perspective article in Proc. Nat. Acad. Sci. (USA) 102, 6671 (2005).
2. M. Moseler and U. Landman, "Formation, Stability and Breakup of Nanojets", Science 289, 1165 (2000); W. Kang and U. Landman, Phys. Rev. Lett. (2006).
3. J. Gao, W.D. Luedtke, D. Gourdon, M Ruths, J.N. Israelachvili, U. Landman, "Frictional Forces and Amontons' Law: From the Molecular to the Macroscopic Sca-

le", J. Phys. Chem. B 108, 3480 (2004).

4. R. N. Barnett, C. L. Cleveland, A. Joy, U. Landman, G. B. Schuster, "Charge Migration in DNA: Ion- Gated Transport", Science 294, 567 (2001); R. N. Barnett et. al., "Oxidative Damage to DNA: Counter Ion- Assisted Addition of Water to Ionized DNA", J. Am. Chem. Soc. (in press, 2006).

Membrane fluctuations around inclusions

Christian D. Santangelo¹ and Oded Farago²

¹Department of Physics and Astronomy, University of Pennsylvania, Philadelphia, PA 19104, USA. e-mail: santancd@sas.upenn.edu. ²Department of Biomedical Engineering, Ben Gurion University, Be'er Sheva 84105, Israel. e-mail: ofarago@bgu.ac.il

ABSTRACT

The free energy cost of inserting a protein into a membrane is determined by considering the variation in the spectrum of thermal fluctuations in response to the presence of a rigid inclusion. Both numerically and through a simple analytical approximation, we find that the primary effect of fluctuations is to reduce the effective surface tension, hampering the insertion at low surface tension. For transmembrane proteins the free energy penalty due to this effect can be quite significant of the order of $10\text{-}20k_B T$, which is comparable but of opposite sign to the previously calculated free energy. Thus, Our results, which should also be relevant for membrane pores, suggest (in contrast to classical nucleation theory) that a *finite* surface tension is necessary to facilitate the opening of a pore.

Bilayer membranes are self-assembled thin fluid sheets of amphiphilic molecules. They are characterized by small bending and large compression moduli, whose effective values are influenced by thermal fluctuations. The softness of the bending modes permit large shape deformations which are important for the biological activities of some living cells (e.g., the red blood cell). Biological membranes are typically highly heterogeneous: they usually consist of mixtures of different lipids and, in addition, contain a variety of different proteins which carry out diverse tasks such as anchoring the cytoskeleton, opening ion channels, and cell signaling.

Membrane inclusions can modify the thermal fluctuations of the membrane by perturbing the local structure of the lipid matrix. It is well-known that the restrictions imposed on the thermal fluctuations of the membrane are the origin of attractive van der Waals-like forces between inclusions [1]. While these long-range interactions are typically very small, they are believed to play an important role in determining the phase behavior (e.g. aggregation) of such systems. Perturbing the spectrum of thermal fluctuations is also expected to contribute to the free energy associated with the insertion of proteins into lipid bilayers, which determines the distribution of proteins between the membrane and the embedding solution. Remarkably, this important entropic contribution to the insertion free energy of a *single* protein has been ignored in previous calculations [2]. In this letter we wish to fill this gap in the literature and study the free energy cost of inserting a rigid inclusion into a membrane, explicitly taking into account effects due to membrane fluctuations. These effects will turn out to be quite significant. At low surface tension they can greatly reduce the the thermodynamic stability of the embedded proteins. Our results should also be relevant for the fluctuation spectrum and nucleation energy of a membrane pore - a different type of local perturbation of the structure of lipid bilayers.

We consider a bilayer membrane consisting of a fixed number of lipids N that spans a planar circular frame of a total area $A_p = \pi L_p^2$, in which a rigid inclusion of radius $r_0 \ll L_p$ has been inserted. The Helfrich energy (to quadratic order) for a nearly-flat membrane in the Monge gauge is given by

$$\mathcal{H}_1 = \sigma A_p + \frac{1}{2} \int d^2\vec{r} \left[\sigma (\nabla h)^2 + \kappa (\nabla^2 h)^2 \right], \quad (1)$$

where σ is the surface tension, κ the bending rigidity, and h the height of the membrane above the frame reference plane. The boundaries of integration in Eqn.(1) include the outer (frame, $r = L_p$) boundary and the inner (inclusion, $r = r_0$) edge. The Laplacian in the Helfrich energy requires that we have two boundary conditions (BCs) for each boundary. On the inner boundary we fix the height of the membrane $h(r_0) = H(\phi)$ and the contact slope $\partial h(r_0)/\partial r = H'(\phi)$, where ϕ is the polar angle measured from the inclusion's axis of symmetry. On the outer boundary we have the natural BCs: $h(L_p) = 0$ and $\nabla^2 h(L_p) = 0$. The particular choice of outer BCs does not modify the free energy of the system in the thermodynamic limit.

To gain insight into the contribution of thermal fluctuations to the insertion free energy we write the height function as $h = h_0 + f$ where h_0 is the extremum of Hamiltonian (1), i.e.,

$$-\sigma \nabla^2 h_0 + \kappa \nabla^4 h_0 = 0, \quad (2)$$

subject to the BCs that $h_0(r_0) = H(\phi)$, $\partial h_0(r_0)/\partial r = H'(\phi)$, $h_0(L_p) = 0$, and $\nabla^2 h_0(L_p) = 0$. This implies $f(r_0) = 0$ and $\partial f(r_0)/\partial r = 0$ on the inner boundary, and $f(L_p) = 0$ and $\nabla^2 f(L_p) = 0$ on the outer boundary. The Helfrich energy can be written as

$$\begin{aligned} \mathcal{H}_1(h_0 + f) = & \sigma A_p + \int d^2\vec{r} \left\{ \frac{1}{2} \left[\sigma (\nabla h_0)^2 + \kappa (\nabla^2 h_0)^2 \right] \right. \\ & \left. + \left[\sigma \nabla h_0 \cdot \nabla f + \kappa \nabla^2 h_0 \nabla^2 f \right] + \frac{1}{2} \left[\sigma (\nabla f)^2 + \kappa (\nabla^2 f)^2 \right] \right\}. \end{aligned} \quad (3)$$

For the cross term (third term in \mathcal{H}_1) we obtain, upon integration by parts,

$$\begin{aligned} \int d^2\vec{r} \left[\sigma \nabla h_0 \cdot \nabla f + \kappa \nabla^2 h_0 \nabla^2 f \right] = & \int d^2\vec{r} \left[-\sigma \nabla^2 h_0 + \kappa \nabla^4 h_0 \right] f \\ & + \int_{\partial M} \kappa \nabla^2 h_0 (\hat{n} \cdot \nabla) f + \int_{\partial M} (\hat{n} \cdot \nabla) \left[\sigma h_0 - \kappa \nabla^2 h_0 \right] f, \end{aligned} \quad (4)$$

where the last two integrals in the above equation are performed on the boundaries of the system, and \hat{n} is a unit vector normal to the boundaries. The boundary terms in Eqn.(4) vanish since $f = 0$ and $\hat{n} \cdot \nabla f = -\partial f/\partial r = 0$ on the inner boundary, and $f = 0$ and $\nabla^2 h_0$ on the outer boundaries. The bulk term also vanishes by virtue of Eqn.(2).

Without the cross term in Eqn.(3), we are left with three terms: the projected area term σA_p , the equilibrium term depending on h_0 , and the fluctuation term depending on f . Thus, the energies associated with h_0 and f completely decouple and their contributions to the free energy are additive. Note that in our approach the equilibrium part of the free energy includes a contribution from the height and tilt fluctuations of the *inclusion*. It is obtained by calculating the dependence of h_0 on the boundary values $H(\phi)$ and $H'(\phi)$, and performing an appropriate thermal average over these quantities. Other energetic components, such as hydrophobicity, translational entropy, electrostatics, should be added to the equilibrium term, and can be included in its definition [3]. The equilibrium

term has been analyzed in many previous studies [2]. Its magnitude is protein specific and is usually in the range of -5 to $-20k_B T$ [4]. In contrast, the effect of *membrane* fluctuations on the insertion free energy has not yet been considered in the literature. We proceed to calculate the fluctuation part of the insertion free energy. Note that it is independent of the height and the contact angle of the inclusion (and their thermal fluctuations), which affect only the equilibrium part¹.

Neglecting the equilibrium term, we are left with the projected area and the fluctuation terms. By integrating the latter by parts twice, the remaining Hamiltonian takes the form

$$\mathcal{H}_2(f) = \sigma A_p + \frac{1}{2} \int d^2\vec{r} f (-\sigma \nabla^2 + \kappa \nabla^4) f. \quad (5)$$

The boundary terms vanish in the above expression due to our choice of BCs: $f(r_0) = 0$, $\partial f(r_0)/\partial r = 0$, $f(L_p) = 0$, and $\nabla^2 f(L_p) = 0$. We proceed by expanding the function f in a series of eigenfunctions $f_{m,n}(r)$ of the operator $\mathcal{L} \equiv -\sigma \nabla^2 + \kappa \nabla^4$: $f(r, \phi) = \sum_{m,n} h_{m,n} f_{m,n}(r) e^{im\phi}$. The functions $f_{m,n}(r)$ can be written as the linear combination of the Bessel functions, $J_m(r)$ and $Y_m(r)$, of the first and second kinds of order m , and the modified Bessel functions of the first and second kinds of order m , $K_m(r)$ and $I_m(r)$:

$$f_{m,n}(r) = AJ_m(\lambda_1^{m,n} r) + BY_m(\lambda_1^{m,n} r) + CK_m(\lambda_2^{m,n} r) + DI_m(\lambda_2^{m,n} r),$$

where the λ_i ($i = 1, 2$) are the positive solutions of $(-1)^{i+1} \sigma (\lambda_i^{m,n})^2 + \kappa (\lambda_i^{m,n})^4 = \mu_{m,n}$, and $\mu_{m,n}$ is the eigenvalue corresponding to the function $f_{m,n}(r)$: $\mathcal{L} f_{m,n}(r) = \mu_{m,n} f_{m,n}(r)$.

Applying the BCs at r_0 and L_p , we derive the eigenvalue equation

$$\lambda_1 [I_m(\lambda_2 r_0) K_m(\lambda_2 L_p) - I_m(\lambda_2 L_p) K_m(\lambda_2 r_0)] [Y'_m(\lambda_1 r_0) J_m(\lambda_1 L_p) - J'_m(\lambda_1 r_0) Y_m(\lambda_1 r_0)] = \lambda_2 [K'_m(\lambda_2 r_0) I_m(\lambda_2 L_p) - I'_m(\lambda_2 r_0) K_m(\lambda_2 L_p)] [J_m(\lambda_1 r_0) Y_m(\lambda_1 L_p) - J_m(\lambda_1 L_p) Y_m(\lambda_1 r_0)] \quad (6)$$

(for brevity, we have omitted the superscript (m, n) from the notation of the λ_i in the above equation). In contrast, for membranes without inclusions, we solve the simple equation $J_m(\lambda_1 L_p) = 0$. It is interesting to note that, in the limit that $\lambda_1^{m,n} r_0 \ll |m|$, Eqn.(6) reduces to the eigenvalue equation in the absence of inclusions. This has the physically appealing interpretation that modes with characteristic lengths much larger than the inclusion radius are hardly perturbed by its presence. In the opposite limit, $\lambda_1^{m,n} r_0 \gg |m|$ (which also implies $\lambda_1^{m,n} L_p \gg |m|$), we can neglect terms proportional to $I_m(\lambda_i^{m,n} L_p)$ (which, otherwise, become exponentially large) and replace the remaining Bessel functions by their leading order asymptotic expressions. This gives, for $\lambda_1^{m,n} \gg \sqrt{\sigma/\kappa}$, the simple equation $\tan[\lambda_1^{m,n} (L_p - r_0)] = 1$, and the solutions $\lambda_1^{m,n} \approx [|m|/2 + n + (-1)^m \pi/4] \pi / (L_p - r_0)$. The physical interpretation of this result is that the inclusion acts like a hard wall for modes with characteristic lengths much smaller than its radius. The effective linear size of the membrane for these modes is reduced from L_p to $L_p - r_0$ and the eigenvalues in this regime increase by roughly a factor of $L_p / (L_p - r_0)$. Thus, the dominant effect of

¹The inner boundary reflects the projection of the cross-sectional area of the inclusion onto the frame reference plane. In the above derivation, we consider a circular boundary with a fixed radius $r = r_0$. However, the locus of the inner boundary depend on the tilt angle of the inclusion and varies accordingly. A straightforward calculation [7] shows that if the tilt angle is small (i.e., when the inner boundary only slightly deviates from circularity) then the boundary of integration in Eqn.(1) can be still taken as circular at the expense of introducing an additional boundary term in the Hamiltonian. The new boundary term has no influence on the membrane fluctuations which are governed by the surface Hamiltonian only. Therefore, and for the sake of the simplicity of our derivation, we have dismissed this extra boundary term and its derivation from the discussion.

the inclusion on the short wavelength modes is to lower the density of contributing modes in “ λ -space” [Note that $\lambda_1^{m,n+1} - \lambda_1^{m,n} = \pi/(L_p - r_0)$].

When the function $f(r, \phi) = \sum_{m,n} h_{m,n} f_{m,n}(r) e^{im\phi}$ is substituted in Hamiltonian (5), we find, due to the orthogonality the eigenfunctions

$$\int_0^{2\pi} d\phi \int_{r_0}^{L_p} r dr f_{m_1, n_1}(r) f_{m_2, n_2}(r) e^{i(m_1+m_2)\phi} = a_0 \delta_{m_1, -m_2} \delta_{n_1, n_2}, \quad (7)$$

that the modes decouple and that the Hamiltonian takes a quadratic form in the amplitudes $|h_{m,n}|$. The normalization coefficient a_0 in Eqn.(7) is the projected area per amphiphilic molecule in the bilayer. Tracing over $|h_{m,n}|$ leads to the following expression for the Gibbs free energy associated with Hamiltonian \mathcal{H}_2 [5]

$$G(\sigma, A_p) = \sigma A_p + \frac{k_B T}{2} \sum_{m,n} \ln \left\{ \frac{[\sigma(\lambda_1^{m,n})^2 + \kappa(\lambda_1^{m,n})^4] A_p \lambda_{dB}^2}{2\pi k_B T N} \right\}, \quad (8)$$

where λ_{dB} is the thermal de-Broglie wavelength of the lipids. The Helmholtz free energy is given by $F(A, A_p) = G - \sigma A$, where the total membrane area A is related to the surface tension by ²

$$A \simeq A_p + \frac{k_B T}{2} \sum_{m,n} \frac{1}{\sigma + \kappa(\lambda_1^{m,n})^2}. \quad (9)$$

Assuming that the membrane is incompressible and, therefore, that its total area is fixed, we can use Eqn.(9) to derive the following equation, relating the surface tension and the inclusion’s radius

$$-\pi r_0^2 + \frac{k_B T}{2} \sum_{m,n} \frac{1}{\sigma + \kappa(\lambda_1^{m,n})^2} - \frac{1}{\sigma_0 + \kappa(\lambda_{1,(0)}^{m,n})^2} = 0. \quad (10)$$

In the above equation $\lambda_{1,(0)}^{m,n}$ are the corresponding solutions of the eigenvalue equation in the absence of the inclusion ($r_0 = 0$): $J_m(\lambda_{1,(0)}^{m,n} L_p) = 0$, and $\sigma_0 \equiv \sigma(r_0 = 0)$. The solution to Eqn.(10) has the form

$$\sigma = \sigma_0(1 + \delta), \text{ where } \delta \sim \mathcal{O}(r_0/L_p)^2. \quad (11)$$

The projected area and fluctuation parts of the insertion free energy $\Delta F(r_0) \equiv F(r_0) - F(0)$ can now be calculated using Eqs.(8) and (10). We find that $\Delta F(r_0)$ is given by

$$\Delta F(r_0) \approx -\pi \sigma_0 r_0^2 + \frac{k_B T}{2} \sum_{m,n} \ln \left[\frac{\sigma_0(\lambda_1^{m,n})^2 + \kappa(\lambda_1^{m,n})^4}{\sigma_0(\lambda_{1,(0)}^{m,n})^2 + \kappa(\lambda_{1,(0)}^{m,n})^4} \frac{L_p^2 - r_0^2}{L_p^2} \right]. \quad (12)$$

Note that only σ_0 appears in the above expression, which is due to Eqn.(11) and the fact that we attempt to calculate $\Delta F(r_0)$ only up to quadratic order in r_0/L_p . For the same reason we can use σ_0 rather than σ in the eigenvalue equation (6). The surface tension appears implicitly in this equation, through the relation $\lambda_2^2 = \lambda_1^2 + \sigma/\kappa$. In expression (12) we assume that the number of molecules forming the bilayer membrane does not change with the insertion of the protein. Consequently, the total number of modes which is directly proportional to the number of molecules in the bilayer is kept constant. In contrast, the projected area per molecule [which appears in Eqn.(7)] does depend on the

²Corrections to this relation can be neglected when the tilt angle and height of the membrane on the inner boundary are small: $H' \ll 1$, $HH' \ll r_0$.

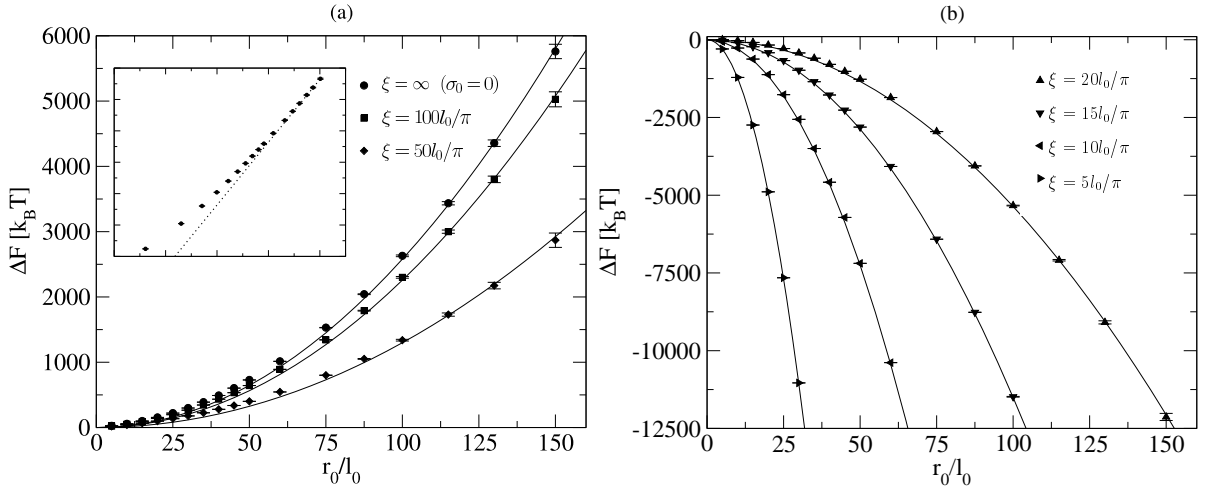


Figure 1: The insertion free energy ΔF as a function of the inclusion's radius for $\kappa = 10k_B T$ and various values of σ_0 . The inset to graph (a): a log-log plot of the numerical results for $\sigma_0 = 0$. The slope of the straight dotted line is 2.

radius of the inclusion, and this is the origin of the term $(L_p^2 - r_0^2)/L_p^2$ appearing in the argument of the logarithm in Eqn.(12). The first term on the right hand side (r.h.s.) of Eqn.(12) comes from the reduction of the projected area. We will now show that, to a good approximation, the second term on the r.h.s. of Eqn.(12) is quadratic in r_0 and, thus, can be interpreted as a thermal correction to the surface tension.

In order to obtain an analytical result for the free energy (12), we make the approximation [based on our discussion of the asymptotic behavior of the eigenvalues $\lambda_1^{m,n}$, see the text after Eqn.(6)] that eigenvalues such that $\lambda_1^{m,n} r_0 < \alpha|m|$ (long wavelength) are not affected by the inclusion, whereas modes with $\lambda_1^{m,n} r_0 > \alpha|m|$ (short wavelength) grow by a factor $L_p/(L_p - r_0)$. The numerical constant α is of the order of unity and its value, which may depend on the surface tension σ_0 , will be determined later by an exact numerical evaluation of ΔF . We have verified numerically that this asymptotic form is indeed correct. We set $n = 0, 1, \dots, \sqrt{N_0}$, and, $m = -\sqrt{N_0}, \dots, \sqrt{N_0}$ so that the total number of modes (degrees of freedom), $2N_0$, is proportional to the number of molecules forming the membrane, N . Along with these approximations, we evaluate the sum in equation (12) as an integral, giving us the simple result (correct up to quadratic order in r_0) that $\Delta F = -\pi(\sigma_0 - \sigma^*)r_0^2$, where

$$\sigma^* = \frac{k_B T}{\pi \alpha \ell_0^2} \left\{ 2 - \alpha - \left(\frac{\ell_0}{\pi \xi} \right)^2 \ln \left[\left(\frac{\pi \xi}{\ell_0} \right)^2 + 1 \right] \right\}, \quad (13)$$

$\xi = \sqrt{\kappa/\sigma_0}$, and $\ell_0 = L_p/\sqrt{N_0}$ is a microscopic length cutoff on the order of the characteristic size of a membrane molecule. We thus obtain the result that the fluctuations renormalize the surface tension. It is interesting to note that this renormalization tends to occur with the opposite sign as the bare surface tension (for $\ell_0 \lesssim \xi$), thus making it *harder* to insert an inclusion. Only for very stressed membrane ($\xi \lesssim \ell_0$) does σ^* become negative. This is due to the reduction of the projected area that allows more thermal fluctuations. A more careful analysis of the long wavelength modes shows that these contribute only finite-size effects to the free energy which vanish in the limit of $L_p \gg r_0$.

We have numerically solved the eigenvalue equation (6) and used the solutions to evaluate the sum in Eqn.(12). Numerical values of $\Delta F(r_0)$ (for $\kappa = 10k_B T$ and various

values of σ_0) are shown in Fig.1 (a)-(b). They have been extracted by extrapolating the numerical results obtained for several values of $750 \leq N_0 \leq 2000$ to the thermodynamic limit $N_0 \rightarrow \infty$. In the inset to Fig.1 (a), the results for $\sigma_0 = 0$ are replotted on a logarithmic scale, showing that our prediction of a quadratic relation between ΔF and r_0 is attained only for large inclusions with $r_0 \gtrsim 100\ell_0$ (the slope of the straight dotted line is 2). This is a typical size for colloidal particles [6]. The value of the constant α appearing in Eqn.(13) shows a slight dependence on the surface tension varying from 1.59 for $\sigma_0 = 0$ to 1.72 for $\xi = \sqrt{\kappa/\sigma_0} = 5\ell_0/\pi$. The solid curves in Fig.1 (a)-(b) depict our analytical expression for ΔF , with α determined by fitting the results for large r_0 to Eqn.(13). From Fig.1 (a) we conclude that, because of thermal fluctuations, there is a free energy penalty to embedding an inclusion in a weakly stretched membrane (small σ_0). For transmembrane proteins with typical radii of $r_0 \lesssim 5\ell_0$, the energy cost is $\Delta F \lesssim 25k_B T$, which is comparable to the equilibrium contribution but of opposite sign. This demonstrates the importance of the membrane fluctuations in determining the distribution of transmembrane and free proteins. For larger inclusions, the fluctuation free energy will dominate the equilibrium part. On the other hand, Fig.1 (b) shows that inclusions greatly reduce the free energy of strongly stretched membranes (large σ_0). The primary reason that the free energy is lowered in this regime is the reduction of the projected area. These results should also be relevant for the question of nucleation of a membrane pore which, albeit more complicated, can be studied by similar approach [7]. They suggest that there exists a (finite!) critical value of the surface tension below which pores cannot open and above which they grow without bounds. Classical nucleation theory, which ignores fluctuations effects, predicts that the critical surface tension is zero [8].

In summary, we have computed the free energy of inserting an inclusion into a membrane. We explicitly calculated the contribution of membrane fluctuations. The primary effect of these fluctuations is to reduce the effective value of the surface tension. At low surface tension it provides a positive component to the free energy of an embedded inclusion, thereby impeding the insertion of transmembrane proteins. The sensitivity of the free energy to variations of the surface tension suggests that, by controlling the membrane surface tension appropriately, one may control the thermodynamic stability of embedded proteins and, thus, the equilibrium distribution between proteins inserted in the membrane and in solution.

Acknowledgments: We thank M. Kardar, A.W.C. Lau, and P. Pincus for useful discussions.

References

- [1] R. Bruinsma, P. Pincus, "Protein aggregation in membranes", *Curr. Opin. Solid State Mater. Sci.* **1**, 401 (1996); M. Kardar, R. Golestanian, "The "friction" of vacuum, and other fluctuation-induced forces", *Rev. Mod. Phys.* **71**, 1233 (1999), and references therein.
- [2] S. May, "Theories on structural perturbations of lipid bilayers", *Curr. Opin. Colloid Interface Sci.* **5**, 244 (2000); M.B. Partenskii, P.C. Jordan, "Membrane deformation and the elastic energy of insertion: Perturbation of membrane elastic constants due to peptide insertion", *J. Chem. Phys.* **117** 10768 (2002), and references therein. An exception is the discussion in R.R. Netz, "Inclusions in fluctuating membranes: Exact results", *J. Phys. I (France)* **7**, 833 (1997).

- [3] A. Ben-Shaul, N. Ben-Tal, B. Honig, “Statistical thermodynamic analysis of peptides and protein insertion into lipid membranes”, *Biophys. J.* **71**, 130 (1996).
- [4] T. Lazaridis, “Effective energy function for proteins in lipid membranes”, *Proteins* **52**, 176 (2003), and references therein.
- [5] P. Sens, S. A. Safran, “Pore formation and area exchange in tense membranes”, *Europhys. Lett.* **43**, 95 (1998).
- [6] I. Koltover, J. O. Rädler, C. Safinya, “Membrane mediated attraction and ordered aggregation of colloidal particles bound to giant phospholipid vesicles”, *Phys. Rev. Lett.* **82**, 1991 (1999).
- [7] O. Farago, C.D. Santangelo, “Pore formation in fluctuating membranes”, *J. Chem. Phys.* **122**, 044901 (2005).
- [8] J.D. Litster, “Stability of lipid bilayers and red blood cell membranes”, *Phys. Lett. A* **53**, 193 (1975).

Scanning Probe Microscopy of Cytoskeleton Networks

Agnes Ostafin

University of Utah, Material Science and Engineering - Bioengineering, Center for Molecularly Engineered Materials, 84112 Salt Lake City, USA

The advent of scanning probe microscopies (SPM) suitable for the study of biological specimens at near physiological condition, such as atomic force microscopy (AFM) and near field scanning optical microscopy NSOM provides an intriguing glimpse at the architecture and mechanical properties of complex protein networks of the cell membrane. How these techniques can be used to extract quantitative information at the molecular level about protein networks that would be useful for modeling and identification of specific disease states remains a technological challenge. In this presentation, some of the achievements and challenges of using SPM to study cellular membranes will be reviewed. Our recent work developing a systematic method for quantifying architectural details from AFM images, allows the use of voxel counting to identify comparable specimen images, and pixel histogramming to evaluate the degree of architectural shift as a consequence of disease and mutation in human and murine cytoskeleton assemblies in vitro. The principles behind using surface tension to generate pico-Newton level forces to rupture weak associations will also be described. This method, which generates membrane tension by the specific attachment of membranes to a surface prior to air drying, has been applied to understand the effects of calcium ions, cellular aging, and disease on the resiliency of the cytoskeleton network in vitro.

The Mechanics of Retrovirus Replication Cycle

Itay Rouso

Weizmann Institute of Science, Dept. of Structural Biology, 76100 Rehovot, Israel

Following budding from the host cell, retroviruses undergo a process of internal reorganization called maturation, which is prerequisite to infectivity. Viral maturation is accompanied by dramatic morphological changes, which are poorly understood in physical/mechanistic terms. A study of the mechanical properties of live mature and immature murine leukemia virus and HIV particles by indentation type experiments conducted with an atomic force microscope tip will be presented. We find that both mature and immature particles have a structured shell. Our results are the first analysis of the mechanical properties of an animal virus, and demonstrate a linkage between virus morphology and mechanical properties. More importantly, we find a striking correlation between HIV mechanical properties and its ability to fuse with target cells. Our work establishes the groundwork for further investigation of a possible link between mechanical properties of a virus and biological function.

Theory of cell adhesion and elasticity

S. Safran¹, A. Besser², R. De¹, A. Nicolas³, A. Zemel¹

¹*Dept. Materials and Interfaces, Weizmann Institute of Science, Herzl Street, 76100 Rehovot, Israel*

²*Ruprecht-Karls-University of Heidelberg, URZ, Im Neuenheimer Feld 293, 69120 Heidelberg, Germany*

³*Laboratoire de Physique de la Matière Condensée, UMR 6622, Parc Valrose, 06108 Nice cedex 2, France*

Forces exerted by adherent cells are important for many physiological processes such as wound healing and tissue formation. By pulling on their environment, cells sense rigidity gradients, boundaries and strains induced by the presence of other cells. Cell adhesions are composed of proteins that form condensed domains that grow in the direction of externally applied or internal, cytoskeletal forces. Theoretical models require a multiscale approach beginning with the adsorption dynamics of individual proteins whose collective behavior determines the growth of micron-sized adhesions. The results for this single-cell behavior are then used to predict the elastic properties of an ensemble of cells, each of which is actively exerting forces on an elastic matrix. The adhesion forces generated by a collection of cells in a tissue significantly alter the overall elastic response of the system. We present a theoretical model for the adsorption of adhesion proteins from the cell interior to the adhesion site and predict the resulting, force-sensitive anisotropic growth. The ensemble of cells is treated by introducing the elastic analogy of the dielectric constant of the medium to predict the average cell polarization, their orientational order, and the effective material constants.

Mechanical behavior of single living fibroblasts by micro force sensors

Shengyuan Yang and M. Taher A. Saif

Department of Mechanical and Industrial Engineering, University of Illinois at Urbana-Champaign, 1206 West Green Street, Urbana, Illinois 61801, USA, saif@uiuc.edu

ABSTRACT

The importance of studying the mechanical behavior of single living cells has been recognized. Here, by using a micro force sensor, we measure the detaching force response of a cell from the sensor probe, and observe the response of the actin network due to the disturbance of the sensor probe.

1. Introduction

Living cells are always subjected to mechanical stimuli originating from their extracellular and intracellular environments. They respond to mechanical stimuli not only mechanically but also biologically. Ranging from adhesion strength to stretch/indentation force response, the mechanical behavior of single living cells has been extensively reported for the past 20 years [1]. Adhesion strength between cells and their substrates and between two cells was measured, for example, by shear flow and micropipette aspiration techniques [2,3]. But, monitoring of the force response during the cell detachment is rare. By using a microcantilever to push against a cell, the force-displacement relationship was measured during the detachment process of murine fibroblasts from a substrate [4]. But, the detaching force response during the cell stretch process has not yet been fully explored.

In situ visualization of the response of the actin network inside the cells during mechanical perturbation offers clues on the mechanism of cell force response due to deformation. Heidemann et al. carried out direct observations of the cytoskeleton in green fluorescent protein (GFP)-actin transfected fibroblasts while deforming the cells by glass needles [5]. Kumar et al. quantified the viscoelastic retraction of dissected single living stress fibers in enhanced yellow fluorescent protein (YFP)-actin transfected endothelial cells by a laser nanoscissor [6]. In this paper, we measure the detaching force response during the cell stretch process by a micromachined force sensor. The response of the actin network due to the disturbance of the sensor probe is observed.

2. Materials and Methods

Fig. 1 shows the sensor, which is made of single crystal silicon. Here, the probe is used to contact the cell, and the two fixed-fixed flexible beams are used to measure the cell force response. Each of the beam is 1.96 mm long, 1.18 μm wide (in plane), and 4.99 μm deep. The probe is 5.0 μm wide. The sensor was fabricated by the SCREAM process [7], and the spring constant of the sensor was calibrated as 23 nN/ μm . The cells were monkey kidney fibroblasts (MKFs), cultured from the cell line CV-1 (ATCC). The cells were transfected with the pEGFP-actin vector (BD Biosciences Clontech) to visualize the cytoskeletal actin network

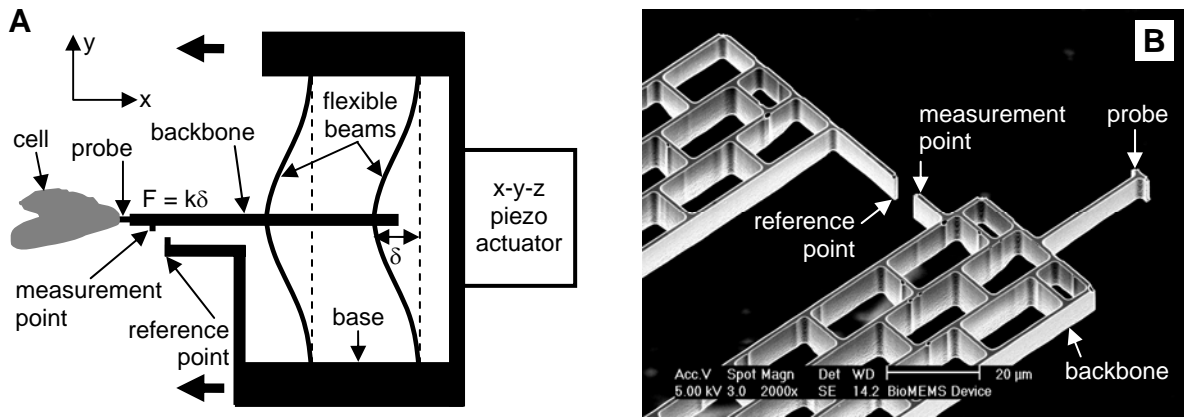


Figure 1. (A) Schematic drawing of the force sensor, and (B) SEM image of its probe part.

inside the cells by fluorescence.

3. Results and Discussion

Fig. 2 shows the measured detaching force response during a cell stretch process by a micromachined force sensor. In this experiment, the probe was coated with RGD (Arg-Gly-Asp) and brought in contact with the cell (initially slightly compressed) to form adhesion between the cell and the probe. The probe was then gradually moved away to detach the cell from the probe by a piezo actuator. The time between any two consecutive data points was kept at 1 min. We see that the detaching force response increases at the initial cell stretch

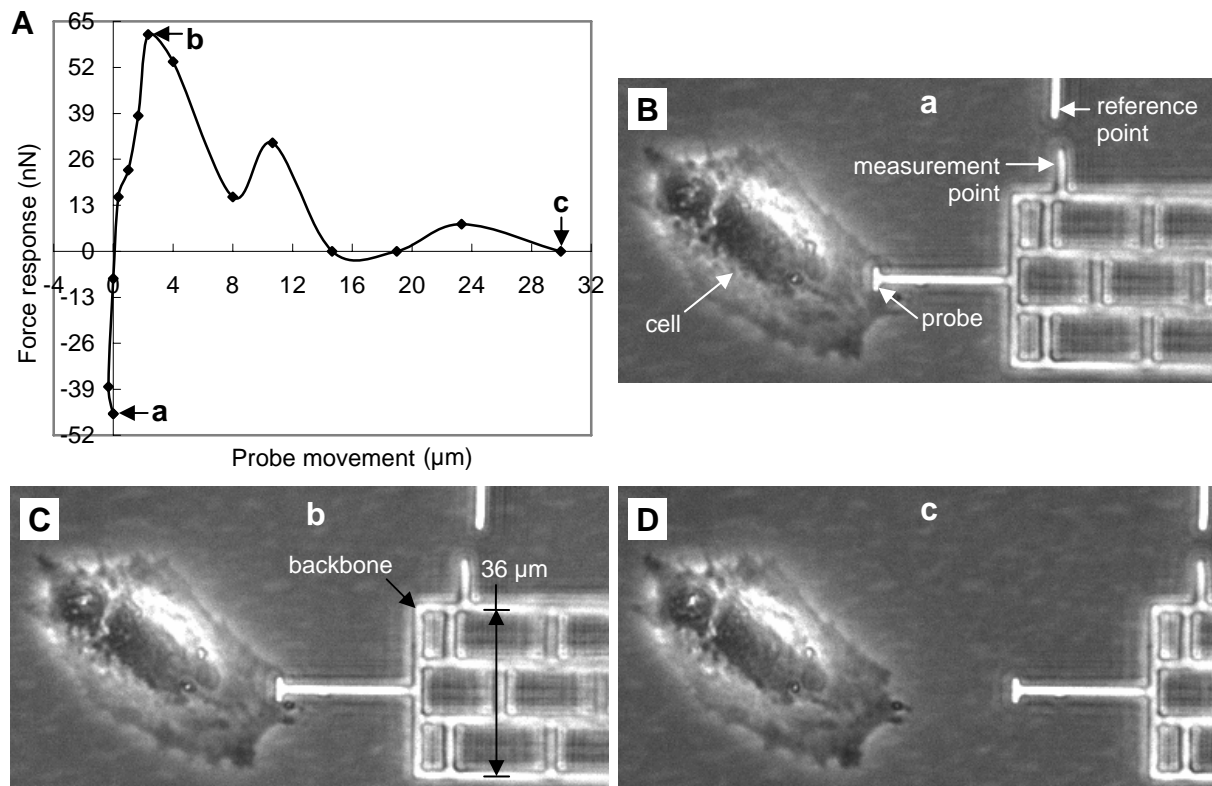


Figure 2. Detaching force response of a fibroblast. (A) Detaching force response versus probe movement, and (B)-(D) Three phase contrast images of the fibroblast and the micro probe. The horizontal misalignment between the measurement point and the reference point shows the deflection of the flexible beams and hence is the measure of the force response.

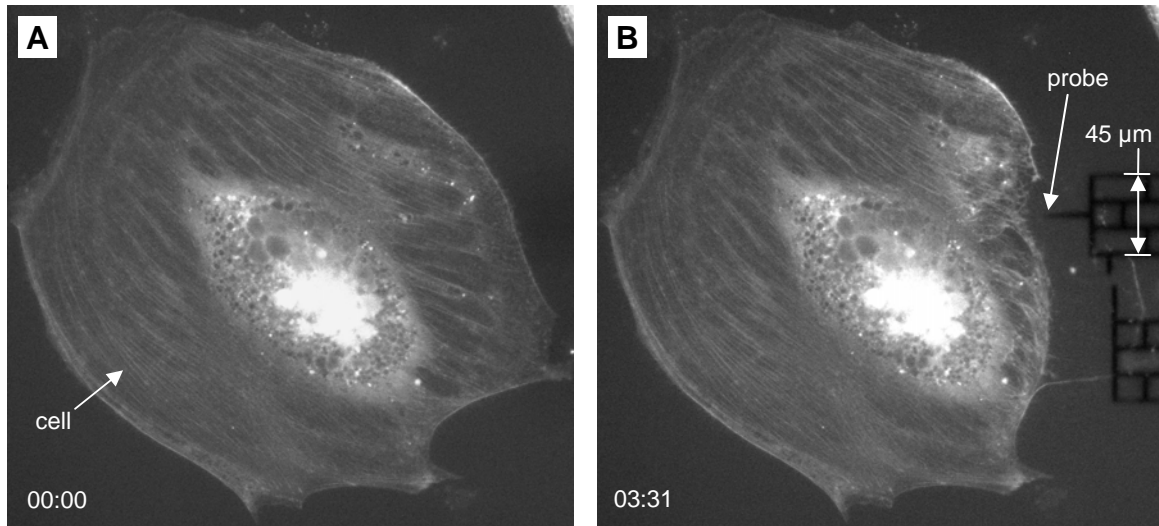


Figure 3. Response of the actin network in an MKF due to the contact of a probe with the cell. The fluorescent images (min:s) are before (A) and after (B) the contact.

stage, then decreases after it reaches its maximum, which may be attributed to the gradual loss of contact between the cell and the probe. The force response of a cell while it is detached from a substrate shows similar characteristics – a force peak followed by a decay over large deformation [4].

In Fig. 3, the sensor probe was positioned above a GFP-actin transfected MKF. The probe was then lower down to gently touch the right most lamellipodium of the cell. Fig. 3A shows the intact actin network of the cell. Fig. 3B shows the actin network 71 s after the touch of the probe. We see, due to the disturbance of the probe, the right most lamellipodium detached from its substrate and contractively curled back towards the central part of the cell body.

4. Conclusions

The detaching force response of a cell from a force sensor micro probe due to stretch has been shown to have a force peak followed by a long force decay tail with displacement. The detachment is thus not abrupt. Contractive curling of stress fibers in the cell due to mechanical contact with the probe is observed.

Acknowledgements

This work was supported by the NSF grants ECS 01-18003 and ECS 05-24675.

References

- [1] G. Bao and S. Suresh, *Nature Mater.* **2**, 715 (2003).
- [2] N. D. Gallant, K. E. Michael, and A. J. Garcia, *Mol. Biol. Cell* **16**, 4329 (2005).
- [3] Y.-S. Chu *et al.*, *Phys. Rev. Lett.* **94**, 028102 (2005).
- [4] A. Yamamoto *et al.*, *Biomaterials* **19**, 871 (1998).
- [5] S. R. Heidemann *et al.*, *J. Cell Biol.* **145**, 109 (1999).
- [6] S. Kumar *et al.*, *Biophys. J.* **90**, 3762 (2006).
- [7] S. Yang and T. Saif, *Rev. Sci. Instrum.* **76**, 044301 (2005).

From DNA to chromatin: the physics of DNA compaction

Martin Depken and Helmut Schiessel

Instituut-Lorentz, Universiteit Leiden, Postbus 9506, 2300 RA Leiden, The Netherlands

ABSTRACT

Chromatin fibers exist in dense and open states, presumably reflecting their corresponding genetic activity. Here we outline a physical theory that describes opening and closing of chromatin fiber as the result of the interplay between electrostatic attraction of nucleosomes and the elasticity of the DNA backbone of the fiber.

1. Introduction

The genomic DNA and the histone proteins compacting it into the chromatin complex comprise most of the contents of the nucleus. In every human cell, for instance, 6×10^9 base pairs (bp) of DNA – corresponding to a total length of about 2 meters – must be packed to fit into a more or less spheroid nuclear volume about $10 \mu\text{m}$ in diameter [1]. Not only has the DNA to be compacted, it also still needs to be accessible to enzymes acting on it, such as replication, transcription and repair machineries, and regulatory factors.

Nature has solved this formidable task by compacting DNA in a hierarchical fashion as schematically depicted in Figure 1. Describing such a complex system with many different length-, time- and energyscales requires a multiscale approach to the problem. The purpose of this conference paper is to outline a first attempt for a self-consistent description of the first three length levels of this hierarchy (DNA, nucleosome, chromatin fiber).

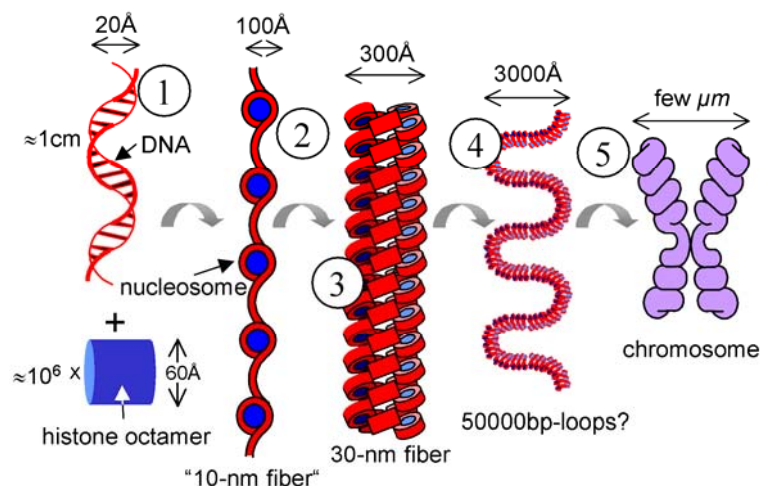


Figure 1. The hierarchical steps of DNA folding into chromatin: (1) DNA (2) “10-nm fiber” and (3) 30-nm chromatin fiber. Details of the higher order structures are largely unknown.

The first step in DNA compaction is the formation of the nucleosome, the elementary chromatin unit: 147 bp DNA wrapped in 1 and 3/4 turns around an octamer of histone

proteins and a section of free linker DNA of 20-80 bp length. The histone octamer with the wrapped DNA, called nucleosome core particle (NCP), has been determined by X-ray crystallography to atomic resolution [2]. At low ionic strengths, the polynucleosome chain forms a bead-on-a-string structure (“10 nm fiber”) that under physiological ionic conditions condenses into a fiber with approximately 30 nm diameter, cf. Fig. 1. Its detailed structure in this state is still under debate.

Two classes of models were proposed for the arrangement of the NCPs inside the 30 nm fiber: the solenoid models [3] and the zig-zag models [4]. In the solenoid model the NCPs are packed one by one along a solenoid helix in the same order as they follow along the chain. The linker DNA is bent in order to allow this geometric arrangement. In the zig-zag model straight linkers connect NCPs located on opposite sides of the fiber. The NCPs are also arranged in a helical order, but neighbors in space are second neighbors along the chain. We will argue that chromatin fibers feature geometries intermediate between those two.

2. Condensation-decondensation transition

The fiber geometry of the zig-zag model can be quantitatively described in terms of two angles: the entry-exit angle $\pi - \theta$ of the linker DNAs at each NCP and the twist angle ϕ between successive NCPs on the chain [5]. For real chromatin fibers those angles vary along the fiber but certain values seem to be preferred. For constant angles we obtain regular fibers as shown in the diagram of states, Fig. 2, with the two axes representing the two angles. Example structures include planar structures for $\phi = 0$ (2-5) and $\phi = \pi$ (6,7), helical arrangements (9) and crossed linker fibers (10). The black area with the intricate boundary corresponds to forbidden structures where NCPs would overlap.

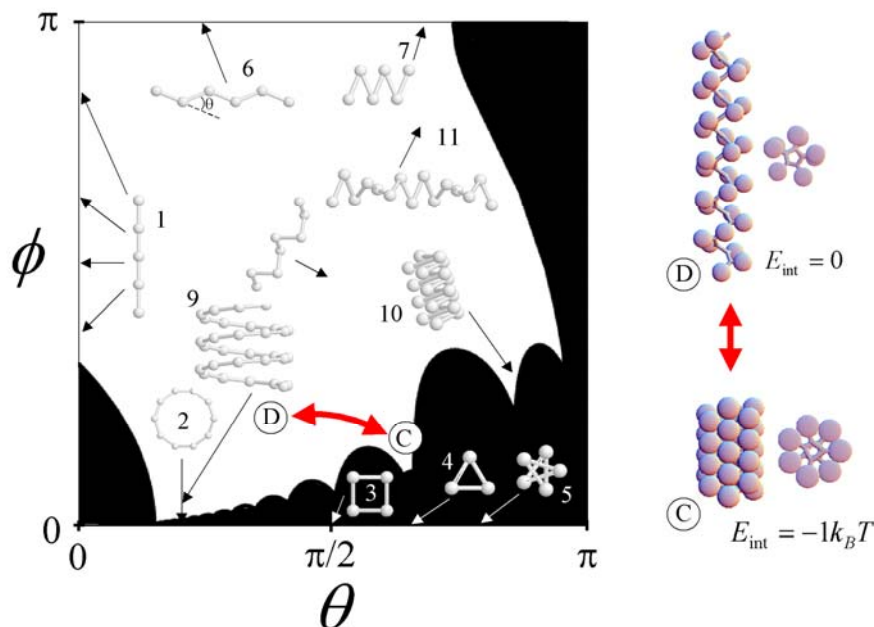


Figure 2. Left: Diagram of two-angle fiber geometries. Right: Fiber condensation-decondensation transition (see text for details).

The two-angle model is purely geometrical. No energies are involved. Clearly this is an oversimplification: NCPs are connected via bendable and twistable DNA linkers. For a given fiber geometry, i.e., a given set of angles (θ, ϕ) , one can analytically calculate all the linear elasticity constant of the DNA linker backbone [1]. A crossed-linker geometry, for instance, features lots of DNA sections crossing back and forth between the NCPs and one finds that

such a fiber is extremely soft, e.g. around 1000 times more extensible than naked DNA (cf. the softness of a normal spring compared to that of the material it is made of). In addition NCPs show electrostatic attraction whose strength is under biochemical control via the acetylation (“uncharging”) and deacetylation (“charging”) of the histone tails, flexible extension of the eight histone proteins [6].

All this indicates that it is necessary to go beyond the simple purely geometric description of the two-angle model and to come to a model that self-consistently takes into account DNA bending, nucleosomal interaction and thermal effects. Here we sketch an approach that is still too naïve for the complexity of the problem but at least gives an idea of some basic issues. A more coherent approach will be presented in the MMM 2006 talk in Freiburg.

For simplicity we here neglect thermal effects that could be brought in at a later stage by assuming a larger effective diameter of the NCPs. Now, even in the absence of thermal fluctuations, i.e. at zero temperature, the fiber geometries with straight linkers given in Fig. 2 do not correspond to ground states *if* the nucleosomes interact energetically with each other. Consider a fiber with a set of values (θ, ϕ) , where the NCPs are not in contact for unbent DNA linkers, corresponding to a structure away from the excluded volume boundary in Fig. 2. Without attraction between the NCPs this fiber is very soft, and would show large shape fluctuations at finite temperatures.

Suppose that we switch now on an attraction between the NCPs. Then, if this attraction is strong enough, the attraction overcomes the DNA linker elasticity and the fiber condenses into a dense fiber with the NCPs in contact, the fiber being located on the excluded volume boundary in Fig. 2. This fiber is very stiff since bending is costly due to the excluded volume of the NCPs. In addition this structure represents a “spring under tension”. Switching off the nucleosomal attraction will lead to a big jump back into the open and soft fiber. This is demonstrated on the rhs of Fig. 2 for a two-angle fiber with $(\theta, \phi) = (0.31\pi, 0.26\pi)$ and linker length 7.14nm . The decondensed fiber (D) corresponds to the ground state for zero-attraction. A condensed fiber (C) occurs for an attraction of $E_{\text{int}} = -1k_B T$ between NCPs in contact that is strong enough to induce a new ground state with densely packed NCPs at new *effective* angles $(\theta_{\text{eff}}, \phi_{\text{eff}}) = (0.67\pi, 0.24\pi)$. It is speculated that such dense fibers with deacetylated, i.e. sticky NCPs, correspond to silent regions without gene expression [7].

Acknowledgements

We thank R. Everaers for helpful discussions.

References

- [1] H. Schiessel, The physics of chromatin, *J. Phys. Condens. Matter* **15**, R699 (2003).
- [2] K. Luger et al., Crystal structure of the nucleosome core particle at 2.8 Å resolution, *Nature* **389**, 251 (1997).
- [3] J. T. Finch and A. Klug, Solenoid model for superstructure in chromatin, *Proc. Natl. Acad. Sci. USA* **73**, 1897 (1976).
- [4] C. L. Woodcock, S. A. Grigoryev, R. A. Horowitz, and N. Whitaker, A chromatin folding model that incorporate linker variability generates fibers resembling native structures, *Proc. Natl. Acad. Sci. USA* **90**, 9021 (1993).
- [5] H. Schiessel, W. M. Gelbart, and R. Bruinsma, DNA folding: structural and mechanical properties of the two-angle model for chromatin, *Biophys. J.* **80**, 1940 (2001).
- [6] F. Mühlbacher, C. Holm, and H. Schiessel, Controlled DNA compaction within chromatin: the tail-bridging effect, *Europhys. Lett.* **73**, 135 (2006).
- [7] P. J. Horn and C. L. Peterson, Chromatin higher-order folding: wrapping up transcription, *Science* **297**, 1824 (2002).

Computational Modeling of Cell and Molecular Mechanics and Human Disease States

Subra Suresh

MIT, Room 4-140, Dept of Materials Science and Engineering, 77 Mass Ave., 02139-4307 Cambridge, United States of America

In this presentation, we provide examples, from our own work and from the literature, of how cell and subcellular mechanics influence, and are influenced by, the onset and progression of human diseases. For this purpose, a broad range of diseases are considered: (1) an infectious disease arising from the invasion of the human erythrocyte by the malaria-causing parasite, *Plasmodium falciparum*, (2) several hereditary hemolytic disorders affecting the human erythrocyte, including sickle cell disease, spherocytosis, elliptocytosis and Asian ovalocytosis, and (3) different types of tumors. In each case, the discussion will focus on how biochemical changes to the appropriate cell type lead to significant molecular reorganization of the intracellular cytoskeleton, and how these changes in turn influence the deformability, cytoadherence and motility of the affected cells. Possible mechanistic origins of disease states in response to these changes are then explored. Particular emphasis will be placed on the role of detailed computational simulations of single-cell and cytoskeletal network deformation on the overall mechanical characteristics, and its dependence and influence on disease states.

Cellular shape formation driven by aggregation of membrane proteins.

Alex Veksler

Department of Chemical Physics, Weizmann Institute of Science, P.O.B. 26, 76100 Rehovot, Israel

Many cell types are not motile but evolve a specific shape, in accordance with their function. One example is the various cells in the brain: from the highly branched neurons to the more compact glial cells. We propose to model the overall cell shape when it is driven by the following mechanisms: (i) some proteins have a spontaneous curvature, hence tending to aggregate on the face of cell membrane and form curved aggregates (buds, invaginations), (ii) when these proteins initiate the growth of actin filaments on the internal side of the membrane, protrusions of various length and width appear on the membrane: dendrites, microvilli, podosomes etc. We propose a continuous non linear model for the protrusions formation which combines the effects of protein interactions, bending dynamics and the driving force of actin polymerization. The relevant length scales vary between a few intermolecular distances and the whole cell. The linear stability analysis and the (nonlinear) perturbation theory were applied to the model. The effect of the essential feedback factors, such as the ATP production and Ca concentration, on the actin growth rate, were examined. The results were compared to the experiments.